Stem Cell Reports
Article

OPEN ACCESS

Generation of Progesterone-Responsive Endometrial Stromal Fibroblasts from Human Induced Pluripotent Stem Cells: Role of the WNT/CTNNB1 Pathway

Kaoru Miyazaki,[1,2] Matthew T. Dyson,[1] John S. Coon V,[1] Yuichi Furukawa,[1] Bahar D. Yilmaz,[1] Tetsuo Maruyama,[2] and Serdar E. Bulun[1,*]

[1]Department of Obstetrics and Gynecology, Feinberg School of Medicine at Northwestern University, Prentice Women's Hospital, 250 E. Superior Street, Room 3-2306, Chicago, IL 60611, USA

[2]Department of Obstetrics and Gynecology, Keio University School of Medicine, Shinjuku, Tokyo 160-8582, Japan

*Correspondence: s-bulun@northwestern.edu

https://doi.org/10.1016/j.stemcr.2018.10.002

SUMMARY

Defective endometrial stromal fibroblasts (EMSFs) contribute to uterine factor infertility, endometriosis, and endometrial cancer. Induced pluripotent stem cells (iPSCs) derived from skin or bone marrow biopsies provide a patient-specific source that can be differentiated to various cells types. Replacement of abnormal EMSFs is a potential novel therapeutic approach for endometrial disease; however, the methodology or mechanism for differentiating iPSCs to EMSFs is unknown. The uterus differentiates from the intermediate mesoderm (IM) to form coelomic epithelium (CE) followed by the Müllerian duct (MD). Here, we successfully directed the differentiation of human iPSCs (hiPSCs) through IM, CE, and MD to EMSFs under molecularly defined embryoid body culture conditions using specific hormonal treatments. Activation of CTNNB1 was essential for expression of progesterone receptor that mediated the final differentiation step of EMSFs before implantation. These hiPSC-derived tissues illustrate the potential for iPSC-based endometrial regeneration for future cell-based treatments.

INTRODUCTION

The endometrium comprises a multilayered mucosa within the uterus. In preparation for the implantation of an embryo, it proliferates, differentiates, degenerates, and regenerates in a cyclical manner in response to ovarian steroid hormones (Maruyama and Yoshimura, 2008; Miyazaki et al., 2012). Estrogen and progesterone bind to their respective receptors ER and PGR and directly regulate the transcription of various genes involved in endometrial physiology. Defective endometrial stromal fibroblast (EMSF) function, particularly abnormal responses to progesterone, play key roles in the development of various types of endometrial disorders, including endometriosis and endometrial cancer. Endometriosis is a painful and persistent gynecological disease that affects approximately 10% of women of reproductive age. Extrauterine growth of endometrium-like tissue results in severe pelvic pain, infertility, and development of adhesions (Bulun, 2009; Dyson et al., 2014; Giudice, 2010; Mahmood and Templeton, 1991). Studies have demonstrated an insufficient response to progesterone in EMSFs from women with endometriosis, which directly affects the stromal-epithelial interactions necessary for normal cycling and function of the endometrium (Kim et al., 2013). Unresponsiveness of EMSFs to progesterone also underlies the pathogenesis of steroid hormone-dependent endometrial cancer (type 1), the most prevalent gynecologic malignancy in the western world, with a rising incidence in the United States (Siegel et al., 2013).

Cell replacement therapies have garnered substantial public and scientific attention as a viable option to replace cells lost or damaged in various disease processes (Daley, 2012; Mutlu et al., 2015). EMSF replacement therapy to restore progesterone responsiveness may similarly provide a novel therapeutic approach to endometrial disease such as endometriosis. The most tractable source of normal EMSFs applicable for clinical use are EMSFs differentiated from patient-derived induced pluripotent stem cells (iPSCs). Human iPSCs (hiPSCs) have been developed using non-integrating episomal factors or synthetic mRNA, producing safer iPSCs with the same efficacy and pluripotency as those derived through viral means (Warren et al., 2010; Yu et al., 2007).

Currently, there is no published method available for differentiating EMSFs from iPSCs. Moreover, the underlying mechanisms for the differentiation of tissue endometrial stem/progenitor cells to EMSFs are not known (Maruyama et al., 2010). We hypothesize that differentiation of iPSCs to EMSFs would mimic the *in vivo* stages of uterine development during embryogenesis. It is also likely that later stages of this process may simulate the steroid-dependent differentiation of tissue progenitor cells to mature endometrial stromal cells. The uterus is a mesodermal organ that originates from the intermediate mesoderm (IM). During embryogenesis, IM emerges from the posterior primitive streak (PS) and gives rise to the coelomic epithelium (CE). Invagination of CE during fetal development forms the Müllerian duct (MD) (Guioli et al., 2007;

Hashimoto, 2003), which then gives rise to the human female reproductive tract, including the oviduct, uterus, and upper vaginal canal (Hashimoto, 2003). Published findings strongly suggest a critical role of the WNT/CTNNB1 pathway in the differentiation of Müllerian tissues (Deutscher and Hung-Chang Yao, 2007; Stewart et al., 2013). Recently, hiPSCs have been differentiated into IM-derived cells that express renal cell lineage markers (Araoka et al., 2014; Morizane et al., 2015), providing a critical starting point for differentiating hiPSCs to EMSFs.

We developed a molecularly defined system for differentiating hiPSCs to EMSFs, whereby embryoid bodies (EBs) of hiPSCs reproducibly recapitulate the hierarchical differentiation stages of PS, IM, CE, and MD. The hiPSC-derived EMSFs expressed the critical endometrial markers HOXA10, HOXA11, and PGR within 14 days of initiation of differentiation (Du and Taylor, 2015; Mote et al., 1999). Prolonged treatment of the hiPSC-derived EMSFs with a time-honored cocktail containing estrogen and progestin, strikingly induced the decidualization (endometrial stromal differentiation) markers FOXO1, HAND2, IGFBP1, and PRL (Buzzio et al., 2006). We predict that histocompatible EMSFs derived from a patients' own cells will permit the development of tailored cell therapies for the endometrial disease. This work represents the first step in developing a cell-based therapeutic approach for women who suffer from uterine factor infertility or endometriosis. The ability to generate functional endometrial tissue from hiPSCs may also create new models for studying endometrial development and pathophysiology, as well as for drug screening. Furthermore, we demonstrate that the WNT/CTNNB1 pathway is a key regulator of *PGR* expression during differentiation of hiPSCs. This finding may be a game changer for novel molecular therapy to improve progesterone resistance seen in a variety of endometrial diseases.

RESULTS

Differentiation of hiPSCs to Intermediate Mesoderm via the Primitive Streak

We differentiated hiPSCs to IM via the posterior PS using a previously established protocol (Figure 1A) (Lam et al., 2014). We first cultured hiPSCs for 1 day in plates with microwells designed to facilitate aggregation of pluripotent stem cells into EBs. Day 1 (D1) EBs were treated for 36 hr with 5 mM CHIR99021 (CHIR), a potent GSK3B inhibitor/CTNNB1 pathway agonist, to generate D2.5 EBs. Transcript levels of *T* and *TBX6*, genes that are predominantly expressed in PS, were significantly higher in D2.5 EBs versus hiPSCs (Figure 1B) (D'Amour et al., 2005; Gadue et al., 2006). Upregulation of T protein was confirmed by immunostaining (Figure 1C) and immunoblot (Figure 1D). Quantitative analysis of the immunohistochemistry revealed that the percentage of T+ cells was significantly higher in D2.5 compared with D1 (94.5% ± 1.0% versus 9.3% ± 2.3%, $p < 0.05$) (Figure S1A). Since it is difficult to perform antigen retrieval followed by immunostaining for plated cells in culture, we used D1 EB for immunostaining in place of hiPSC.

Differentiation of pluripotent stem cells is accompanied by a loss of pluripotency (Lam et al., 2014). Since hiPSCs share many properties with epiblast stem cells (EpiSCs) (Han et al., 2011), we examined the expression of the EpiSC genes *NANOG*, *ZFP42*, and *SOX2*, as well as *KLF4*, a gene used to generate hiPSCs (Takahashi et al., 2007), to verify the pluripotency of the EBs. Decreases in mRNA levels of *NANOG*, *ZFP42*, and *KLF4* were observed in D2.5 EBs compared with hiPSCs (Figure 1B). Downregulation of SOX2 was confirmed by immunostaining (Figure 1C) as the quantitative analysis of immunohistochemistry revealed that the percentage of SOX2+ cells was significantly lower in D2.5 compared with D1 (92.9% ± 1.9% versus 1.4% ± 0.3%, $p < 0.05$) (Figure S1A). Downregulation of NANOG and SOX2 was also confirmed by immunoblot (Figure 1D).

EpiSCs can also differentiate ectoderm cells, early-gastrula organizer, and primordial germ cell precursors as well as PS (Arango and Donahoe, 2008; Davidson and Tam, 2000; Zimmerlin et al., 2017). We evaluated D2.5 EBs for the expression of markers for those derivatives to assess the purity of PS differentiation: *PAX6* for ectoderm (Lam et al., 2014), *LHX1* for early-gastrula organizer (Davidson and Tam, 2000), and *PRDM14* for primordial germ cell precursors (Arango and Donahoe, 2008). We found that mRNA expression was unchanged or downregulated in D2.5 EBs compared with hiPSCs (Figure S1B).

A switch in cadherin protein expression from CDH1 to CDH2 indicates epithelial-mesenchymal transition (EMT) during differentiation of hiPSCs. D2.5 EBs showed decreased expression of CDH1 and increased expression of CDH2 by immunohistochemistry compared with D1 EBs, consistent with cell migration through the PS, as seen during development (Figure 1C) (Ramkumar and Anderson, 2011). Specifically, the quantitative data showed the following: CDH1+, 3.9% ± 0.1% versus 100%, $p < 0.05$; CDH2+, 100% versus 8.3% ± 0.7%, $p < 0.05$ (Figure S1A). Together, these findings demonstrated the potency of CHIR to induce differentiation of hiPSCs into PS-like cells via a program that mimics normal development *in vivo*.

In the next step, D2.5 EBs (PS stage) were treated with 1 mM retinoic acid (RA) and fibroblast growth factor 2 (FGF2) for 36 hr (Figure 1A). We examined whether D4 EBs are committed to the IM lineage by measuring the

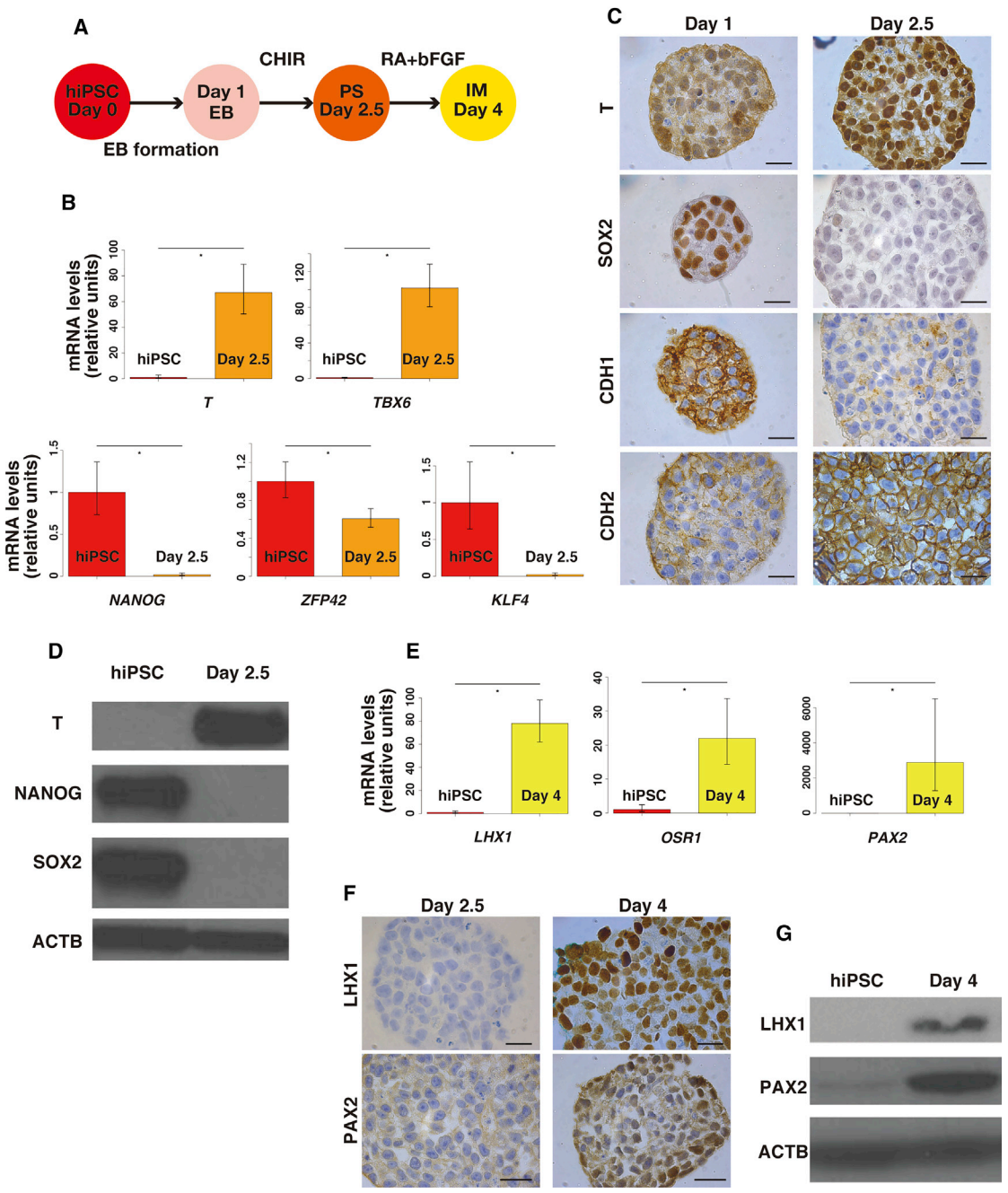

Figure 1. Differentiation of hiPSC into Intermediate Mesoderm via the Primitive Streak

(A) Diagram of differentiation of hiPSCs into IM via PS.

(B) Quantitative RT-PCR of pluripotent stem cell- and PS-specific genes in hiPSCs and day 2.5 EBs. Pluripotent stem cell-specific genes are *KLF4*, *NANOG*, and *ZFP42*, and PS-specific genes are *T* and *TBX6*. Error bars represent RQMin and RQMax (N = 9 independent experiments, *p < 0.05, Student's t test).

(C) Representative images of immunohistochemistry to detect T, SOX2, CDH1, and CDH2 in D1 and D2.5 EBs. Scale bars represent 20 μm.

(D) Representative immunoblot (N = 3 independent experiments) of T, NANOG, and SOX2 in hiPSCs and D2.5 EBs.

(E) Quantitative RT-PCR of IM-specific genes *LHX1*, *OSR1*, and *PAX2* in hiPSCs and day 4 EBs. Error bars represent RQMin and RQMax (N = 9 independent experiments, *p < 0.05, Student's t test).

(F) Representative images of immunohistochemistry to detect LHX1 and PAX2 in D2.5 EBs and D4 EBs. Scale bars represent 20 μm.

(G) Representative immunoblot (N = 3 independent experiments) of LHX1 and PAX2 in hiPSCs and D4 EBs.

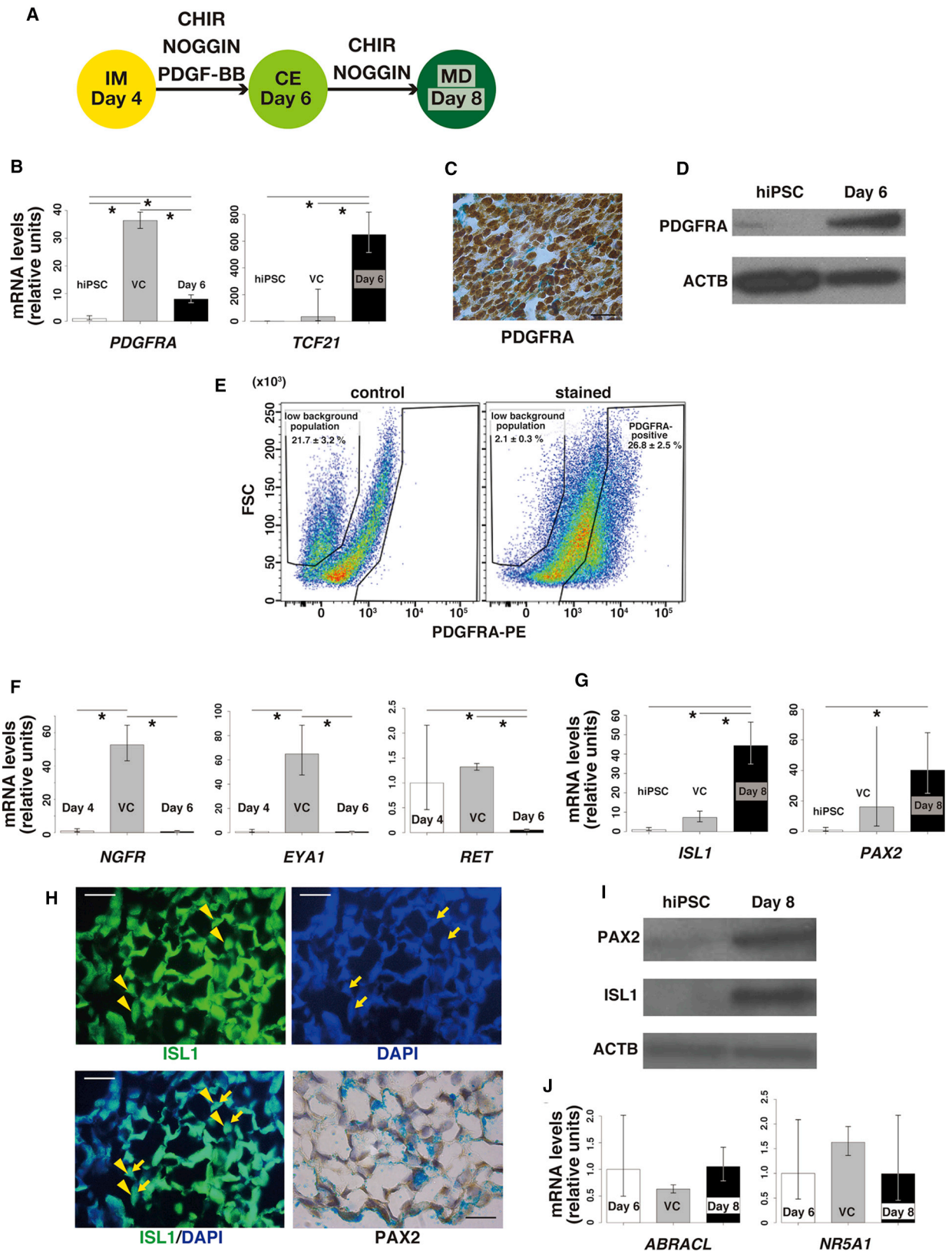

(legend on next page)

expression of LHX1, OSR1, and PAX2, which are expressed in the developing IM (Lam et al., 2014; Mugford et al., 2008). A marked increase in *LHX1*, *OSR1*, and *PAX2* mRNA expression was observed in D4 EBs compared with hiPSCs (Figure 1E). We confirmed protein expression of LHX1 and PAX2 in D4 EBs by immunohistochemistry (Figure 1F) and immunoblot (Figure 1G). Quantitative analysis of the immunohistochemistry revealed that the percentages of LHX1+ cells and PAX2+ cells were significantly higher in D4 compared with D2.5 (96.5% ± 0.5% versus 0%, $p < 0.05$; 96.0% ± 0.6% versus 1.1% ± 1.1%, $p < 0.05$, respectively) (Figure S1C).

Because PS can also give rise to lateral plate mesoderm and hemangioblast (Palpant et al., 2017), we also evaluated the D4 EBs for mRNA expression of markers *GATA4* (Gao et al., 2016) and *CD34* (Young et al., 1995). We found that expression of these markers was downregulated or unchanged compared with D2.5 EBs (Figure S1D). *SOX17*, which is a marker for endoderm originating from the anterior PS (Familari, 2006), was also unchanged in the D4 EBs (Figure S1D). We therefore concluded that D4 EBs were representative of IM.

Differentiation of Intermediate Mesoderm to Coelomic Epithelium

All MD components derive from IM through CE (Hashimoto, 2003), and the WNT/CTNNB1 pathway mediates the development of MD (Deutscher and Hung-Chang Yao, 2007; Stewart et al., 2013). We hypothesized that activation of the WNT/CTNNB1 pathway, in addition to several other growth factors, could reproduce MD development from IM (D4 EBs) *in vitro*. We added the WNT/CTNNB1 pathway activator CHIR, along with NOGGIN and platelet-derived growth factor BB (PDGF-BB), to D4 EB cultures for 2 days (Figure 2A). Because BMP7 is expressed in the Wolffian duct and induces nephrogenesis from IM (Little et al., 2010), we added the BMP antagonist NOGGIN to suppress nephrogenesis. PDGF-BB was added based on its ability to differentiate human embryonic stem cells into Müllerian lineage cells in a previously published protocol (Yu et al., 2015).

To determine whether EB treatment with CHIR, NOGGIN, and PDGF-BB for 2 days induced the development of IM to CE, we examined the expression of CE markers (and lack of IM markers) in treated or untreated (vehicle control) D6 EBs. mRNA levels of *PDGFRA* and *TCF21*, genes that are predominantly expressed in CE (Wilhelm et al., 2007) (Edson et al., 2009), were significantly higher in D6 EBs compared with hiPSCs (Figure 2B) although *PDGFRA* expression was lower in the treated D6 EBs compared with vehicle-control-treated D6 EBs (Figure 2B). Upregulation of PDGFRA protein was confirmed by immunostaining (Figure 2C) and immunoblot (Figure 2D). We used flow cytometry to assess the distribution of PDGFRA-positive cells in D6 EBs. Via plotting forward-scatter (FSC) against fluorescence intensity in the PE channel obtained from the unstained control, we identified two populations: populations with low and high background of PE (Figure 2E). However, in D6 EBs stained with the PDGFRA antibody, 26.8% ± 2.5% of cells were positive for PDGFRA when the positive gate was positioned to exclude the high PE population although the majority of D6 EB cells were PDGFRA positive after immunostaining (Figures 2C and 2E). This may be due to the variable sensitivity of the different antibodies used for each procedure and also the nature of the individual procedures. Addition of

Figure 2. Differentiation of Intermediate Mesoderm into Müllerian Duct

(A) Diagram of differentiation of IM into MD.

(B) Quantitative RT-PCR of coelomic epithelium (CE)-specific genes *PDGFRA* and *TCF21* in hiPSCs and day 6 EBs. Day 6, D6 EBs treated with CHIR, NOGGIN, and PDGF-BB; VC, D6 EBs treated with vehicle control for 2 days, between D4 and D6. Error bars represent RQMin and RQMax. (N = 9 independent experiments except for VC [N = 3 independent experiments], *$p < 0.05$, Student's t test).

(C) Representative image of immunohistochemistry to detect PDGFRA in D6 EBs. Scale bar represents 20 μm.

(D) Representative immunoblot (N = 3 independent experiments) of PDGFRA in hiPSC and D6 EBs.

(E) The representative dot plots of PDGFRA-positive population in cells dispersed from D6 EBs (N = 3 independent experiments).

(F) Quantitative RT-PCR comparing expression of *NGFR*, *EYA1*, and *RET* in D4 EBs and D6 EBs. Day 6, D6 EBs treated with CHIR, NOGGIN, and PDGF-BB; VC, D6 EBs treated with vehicle control, between D4 and D6. Those genes are expressed in non-CE derivatives from IM. Error bars represent RQMin and RQMax (N = 9 independent experiments except for VC [N = 3 independent experiments], *$p < 0.05$, Student's t test).

(G) Quantitative RT-PCR of Müllerian duct (MD)-specific genes *ISL1* and *PAX2* in hiPSC and day 8 EBs. Day 8, D8 EBs treated with CHIR and NOGGIN; VC, D8 EBs treated with vehicle control for 2 days, between D6 and D8. Error bars represent RQMin and RQMax (N = 9 except for VC [N = 3 independent experiments], *$p < 0.05$, Student's t test).

(H) Representative immunofluorescence of ISL1 and immunohistochemistry to detect PAX2 in D8 EB. Scale bars represent 20 μm. Yellow arrowheads indicate nuclear staining of ISL1. Yellow arrows indicate DAPI-positive cell nuclei.

(I) Representative immunoblot (N = 3 independent experiments) for ISL1 and PAX2 in hiPSCs and D8 EBs.

(J) Quantitative RT-PCR comparing expression of *ABRACL* and *NR5A1* in D6 EBs and D8 EBs. Day 8, D8 EBs treated with CHIR and NOGGIN; VC, D8 EBs treated with vehicle control for 2 days, between D6 and D8. Those genes are expressed in non-MD derivatives from IM. Error bars represent RQMin and RQMax (N = 9 independent experiments except for VC [N = 3 independent experiments], *$p < 0.05$, Student's t test).

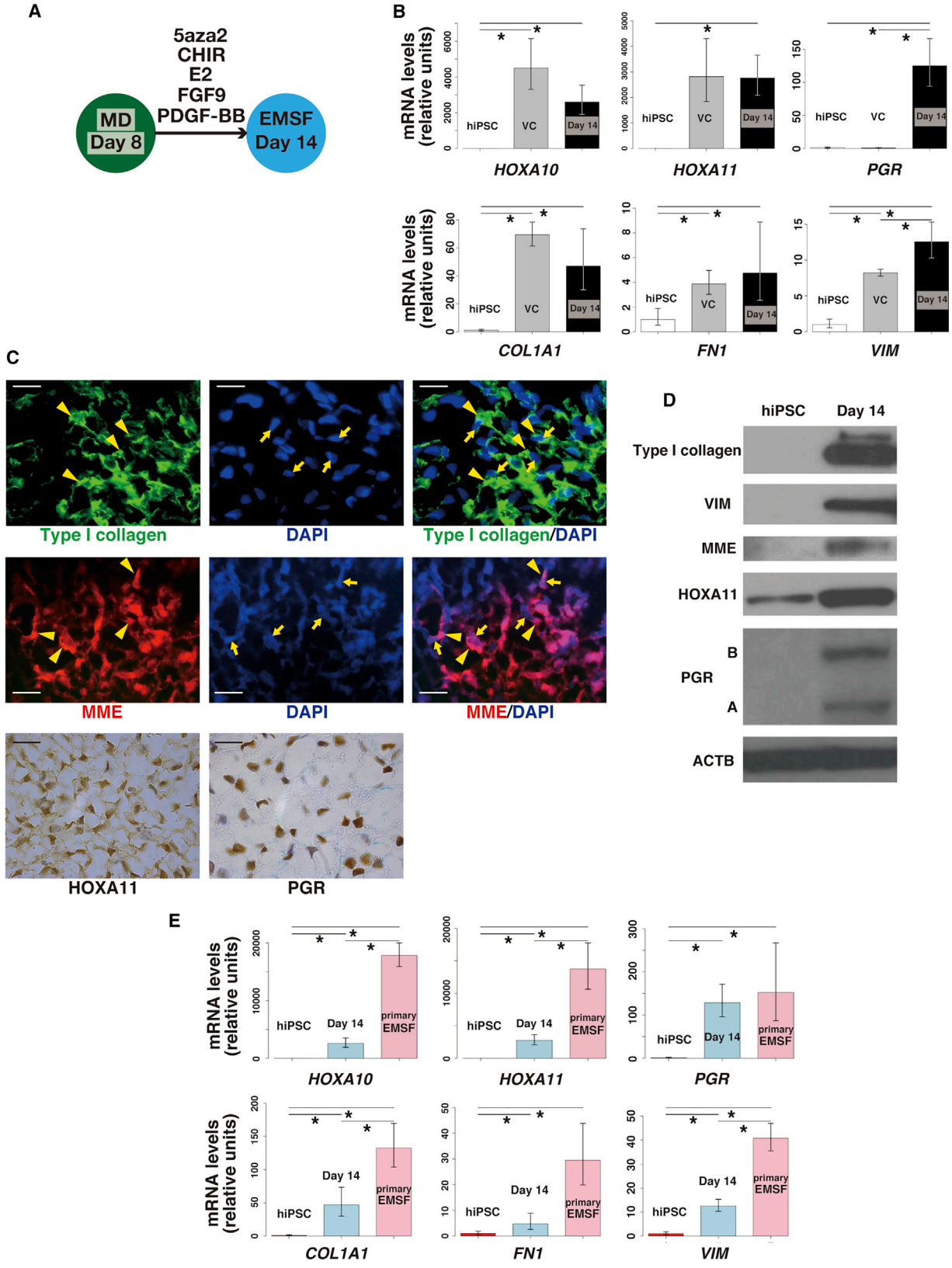

(legend on next page)

CHIR, NOGGIN, and PDGF-BB also significantly suppressed the expression of markers for mesonephros (*NGFR*) (Wilhelm et al., 2007) and metanephric mesenchyme (*EYA1*) (Little et al., 2010) in D6 EBs compared with vehicle-control-treated D6 EBs (Figure 2F). mRNA levels of the Wolffian duct marker *RET* (Little et al., 2010) were not changed among D4 EBs, treated D6 EBs, and vehicle-control-treated D6 EBs (Figure 2F).

Withdrawal of CHIR significantly increased the mRNA levels of *PDGFRA* and *TCF21* (CE markers), but it also enhanced the expression of *EYA1* (metanephric mesenchyme) and *RET* (Wolffian duct) (Figures S1E and S1F), whereas withdrawal of NOGGIN significantly increased the mRNA level of *EYA1* but did not affect the expression of *PDGFRA* or *TCF21* (Figures S1E and S1F). Our data suggested that withdrawal of PDGF-BB enhanced the expression of *EYA1* although there was no statistically significant difference ($p = 0.06$) (Figure S1F). We therefore concluded that the combination of CHIR, NOGGIN, and PDGF-BB is the most optimal cocktail for the differentiation of IM to CE.

We further tested the effects of varying durations of treatment with CHIR, NOGGIN, and PDGF-BB by assaying the expression of differentiation markers from days 5 to 7. Although mRNA levels of *PDGFRA* and *TCF21* were significantly higher in D7 EBs compared with D6 EBs, there was an insignificant trend that D7 EBs expressed more *EYA1* and *RET* compared with D6 EBs ($p = 0.06$) (Figures S1G and S1H). D5 EBs showed significantly higher expression of *EYA1* and *RET* compared with D6 EBs, whereas mRNA levels of *PDGFRA* and *TCF21* were comparable between D5 EBs and D6 EBs (Figures S1G and S1H). We therefore concluded that D6 is the best time point for CE before proceeding to MD.

Differentiation of Coelomic Epithelium into Müllerian Duct

We then cultured D6 EBs with CHIR and NOGGIN for an additional 2 days (i.e., removed PDGF-BB) (Figure 2A), and examined the expression of MD markers and lack of expression of genes typically found in other CE derivatives. mRNA levels of *ISL1* and *PAX2*, genes that are predominantly expressed in MD (Kobayashi and Behringer, 2003), were significantly increased in D8 EBs compared with vehicle control D8 EBs or hiPSCs (Figure 2G). Protein expression of those markers was confirmed by immunostaining (Figure 2H) and immunoblot (Figure 2I). One hundred percent of cells in D6 EBs were ISL1 positive, whereas 90.3% ± 0.8% of cells were PAX2 positive ($N = 3$) (Figure 2H). Conversely, expression of marker genes for other CE derivatives, such as ovarian mesenchymal stroma and testicular interstitial cells (*ABRACL*) (Jameson et al., 2012) and gonadal somatic cells (*NR5A1*) (Edson et al., 2009), was not significantly different among D6 EBs, treated D8 EBs, and vehicle control D8 EBs (Figure 2J). Therefore, we considered the D8 EBs to be a putative MD cell population. Notably, H&E staining revealed a drastic change in cell morphology during the transition from D6 to D8, such that D6 EB cells were primarily "cobblestone" shaped, epithelium-like cells, whereas the majority of cells in D8 EBs were spindle-shaped, fibroblast-like cells (Figure S2).

Differentiation of Müllerian Duct into EMSFs

Next, we cultured D8 EBs with 5′-aza-2′-deoxycytidine (5aza2), CHIR, 17β-estradiol (E_2), FGF9, and PDGF-BB for 6 days (Figure 3A). 5aza2 is a DNA methyltransferase inhibitor that induces pluripotent stem cell differentiation into several cell types (Banerjee and Bacanamwo, 2010; Horrillo et al., 2013). E_2 at a moderate concentration (10^{-8} M) was used to reproduce the levels present in the fetus (Peterson et al., 1975), consistent with a previous protocol used to differentiate human embryonic stem cell into cells of the Müllerian lineage (Yu et al., 2015). FGF9 was added as a known autocrine endometrial stromal growth factor (Tsai et al., 2002), and PDGF-BB was used because it supports clonogenicity of endometrial stromal cells (Chan et al., 2004).

After 6 days of treatment or (vehicle control treatment), we examined whether the D14 EBs had committed to the EMSF lineage based on positive expression of EMSF markers. HOXA10 and HOXA11 are known to play critical

Figure 3. Differentiation of Müllerian Duct into EMSFs

(A) Diagram of differentiation of MD into EMSFs.

(B) Quantitative RT-PCR of EMSF-specific genes *HOXA10*, *HOXA11*, *PGR*, *COL1A1*, *FN1*, and *VIM* in hiPSCs and day 14 EBs. Day 14, D14 EBs treated with 5aza2, CHIR, E_2, FGF9, and PDGF-BB; VC, D14 EBs treated with vehicle control for 6 days, between D8 and D14. Error bars represent RQMin and RQMax ($N = 9$ independent experiments except for VC [$N = 3$ independent experiments], $^*p < 0.05$, Student's t test).

(C) Representative immunofluorescence of type I collagen and MME, and immunohistochemistry to detect HOXA11 and PGR in D14 EB. Scale bars represent 20 μm. Yellow arrowheads indicate intracellular staining of type I collagen or MME staining on cell membranes. Yellow arrows indicate DAPI-positive cell nuclei.

(D) Representative immunoblot ($N = 3$ independent experiments) for COL1A1, VIM, MME, HOXA11, and PGR in hiPSCs and D14 EBs.

(E) Quantitative RT-PCR comparing expression of *HOXA10*, *HOXA11*, *PGR*, *COL1A1*, *FN1*, and *VIM* in hiPSCs, D14 EBs, and primary EMSFs. Error bars represent RQMin and RQMax ($N = 9$ independent experiments except for primary EMSFs [$N = 3$ independent experiments], $^*p < 0.05$, Student's t test).

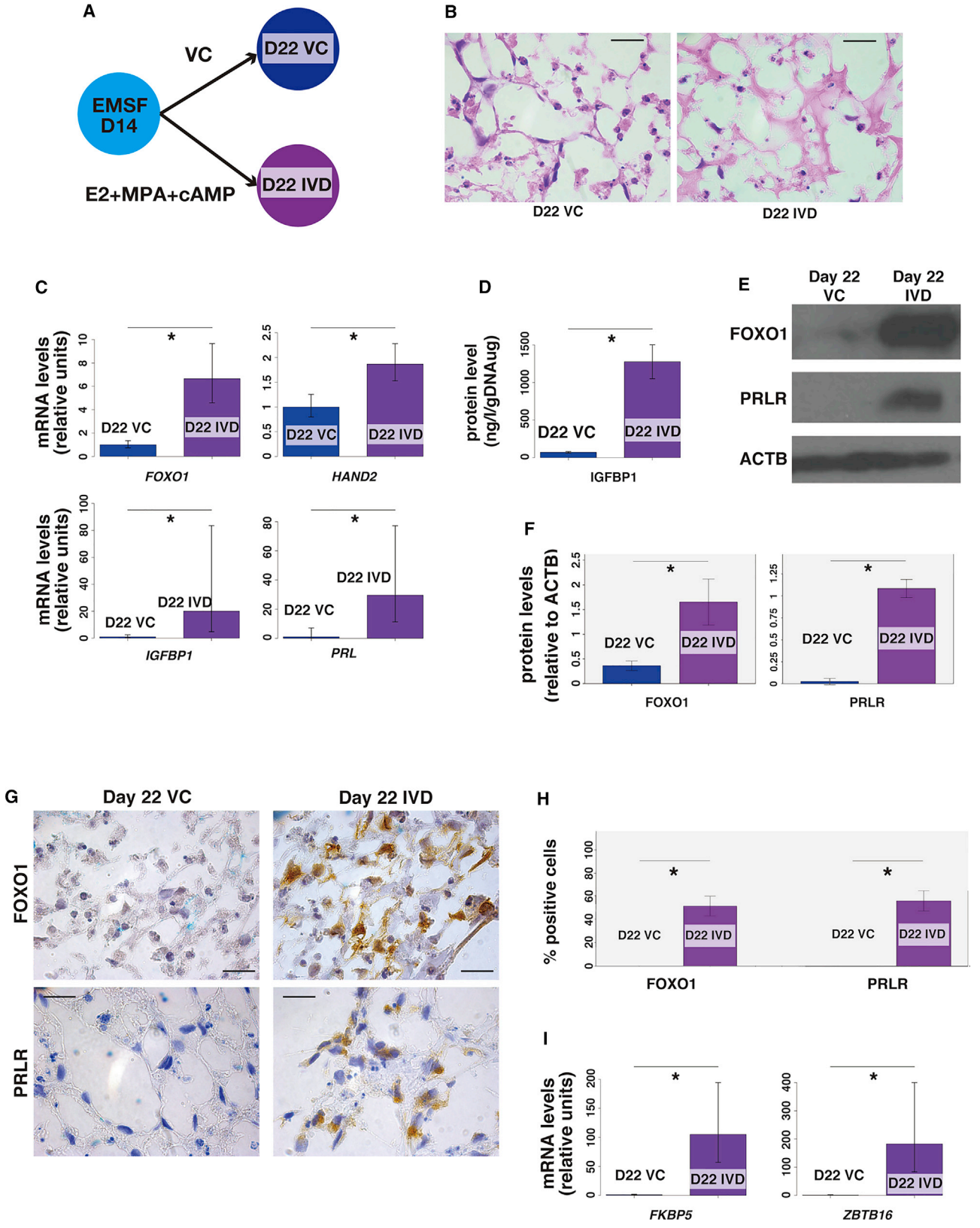

(legend on next page)

roles in developmental patterning of the reproductive tract (Benson et al., 1996; Gendron et al., 1997) and are also necessary for endometrial receptivity (Du and Taylor, 2015). HOXA10 is expressed in the developing uterus (Du and Taylor, 2015) but minimally expressed in fallopian tube tissue (Salih and Taylor, 2004). In fact, the homeotic transformation of the anterior part of the uterus into an oviduct-like structure takes place in response to HOXA10 deficiency (Du and Taylor, 2015). HOXA11 is found in the primordial lower uterus and cervix (Du and Taylor, 2015). MME is a type II transmembrane glycoprotein predominantly expressed in EMSFs (Imai et al., 1992), as is PGR (Mote et al., 1999), which mediates progesterone effects in the endometrium; PGR expression is low in the vagina (Di Carlo et al., 1985). Expression levels of general fibroblast markers, including COL1A1, FN1, and VIMs were also examined (Akamatsu et al., 2013; Busch et al., 2017; Cheng et al., 2016).

mRNA levels of *HOXA10*, *HOXA11*, *PGR*, *COL1A1*, *FN1*, and *VIM* significantly increased in D14 EBs compared with hiPSCs (Figure 3B), although expression of *HOXA10*, *HOXA11*, *COL1A1*, and *FN1* was comparable between treated and vehicle control D14 EBs (Figure 3B). Protein expression of MME, HOXA11, PGR, type I collagen, and VIM was confirmed by immunostaining (Figure 3C) and immunoblot (Figure 3D). One hundred percent of cells in D14 EB were positive for MME and type I collagen, whereas 98.3% ± 1.0% of cells were HOXA11 positive. PGR was expressed in 94.3% ± 1.3% of cells (N = 3) (Figure 3C). Withdrawal of 5aza2 or E_2 between D8 and D14 significantly decreased the expression of EMX2 (Figure S1I), a gene highly expressed in proliferative phase endometrium (Daftary and Taylor, 2004).

Of note, mRNA expression of *PGR* in D14 EBs was comparable with that in cultured primary EMSFs, although expression of *HOXA10*, *HOXA11*, *COL1A1*, and *VIM* in primary EMSFs was significantly higher than that in D14 EBs (Figure 3E). Our data suggested that primary EMSFs also express more *FN1* compared with D14 EBs although there was no statistically significant difference (p = 0.06). The cells in D14 EBs were fibroblast-like cells, with no epithelial glandular formation as shown by H&E staining (Figure S2). Taken together, we considered these cells as an EMSF population.

The transcript levels of *SUSD2*, which is a marker of endometrial mesenchymal stem cells (eMSCs), increases from D4 to D8 (up to 10-fold), and decreases significantly from D8 to D14 (Masuda et al., 2012). This supports the notion that, during the differentiation protocol, these cells acquire some of the eMSC properties at D8, followed by their differentiation to EMSFs, as evident by a decline in *SUSD2* expression (Figure S1J).

D14 EBs Undergo Decidualization in Response to Hormonal Stimulation

During the secretory phase of the human menstrual cycle, EMSFs undergo decidualization in response to hormonal stimulation in preparation for implantation of an embryo (Buzzio et al., 2006). The high levels of expression of PGR in D14 EBs prompted us to further examine the hormone responsiveness of D14 EBs as putative EMSFs. We mimicked the secretory phase hormonal environment in culture to stimulate *in vitro* decidualization (IVD) by treating D14 EBs with E_2, progestin (MPA), and 8-bromoadenosine 3′,5′-cyclic monophosphate (cAMP) (Figure 4A). After 8 days of treatment, there was a significant increase in the cytoplasmic volumes of treated cells, as demonstrated by H&E staining at higher magnification (Figure 4B). Quantification of cytoplasmic area demonstrated the significant increase in the cytoplasmic volume in D22 EBs treated with hormones (D22 IVD) compared with D22 EBs treated with vehicle control (D22 VC) (266.2 ± 29.1 m^2 versus 76.4 ± 4.2 m^2, $p < 0.05$, respectively) (Figure S3A). Furthermore, D22 IVD expressed significantly higher mRNA levels

Figure 4. *In Vitro* Decidualization of D14 EBs

(A) Diagram of *in vitro* decidualization (IVD) protocol in which D14 EBs are treated with E2, MPA, and cAMP (D22 IVD), or with vehicle control (D22 VC) for 8 days, between D14 and D22.

(B) Representative images of H&E staining of D22 VC and D22 IVD. Scale bars represent 20 μm.

(C) Quantitative RT-PCR of decidualization-specific genes *FOXO1*, *HAND2*, *IGFBP1*, and *PRL* in D22 VC and D22 IVD differentiated from clone 1 hiPSCs. Error bars represent RQMin and RQMax (N = 9 independent experiments, *p < 0.05, Student's t test).

(D) ELISA to detect IGFBP1 in D22 VC and D22 IVD. Values are normalized with genomic DNA amount. Error bars represent mean ± SEM (N = 9 independent experiments, *p < 0.05, Student's t test).

(E) Representative immunoblot (N = 3 independent experiments) of FOXO1 and PRLR in D22 VC and D22 IVD.

(F) Immunoblot densities quantified with ImageJ software showing protein levels of FOXO1 and PRLR in day 22 VC and IVD. Data represent means ± SEM (N = 3 independent experiments, *p < 0.05, Student's t test).

(G) Representative images of immunohistochemistry to detect FOXO1 and PRLR in D22 VC and D22 IVD. Scale bars represent 20 μm.

(H) Quantification of cells with positive staining for FOXO1 and PRLR in day 22 VC and IVD. Data represent means ± SEM (N = 3 independent experiments, *p < 0.05, Welch test for FOXO1, Student's t test for PRLR).

(I) Quantitative RT-PCR of PGR-target genes *FKBP5* and *ZBTB16* in D22 VC and D22 IVD. Error bars represent RQMin and RQMax (N = 9 independent experiments; *p < 0.05; Student's t test).

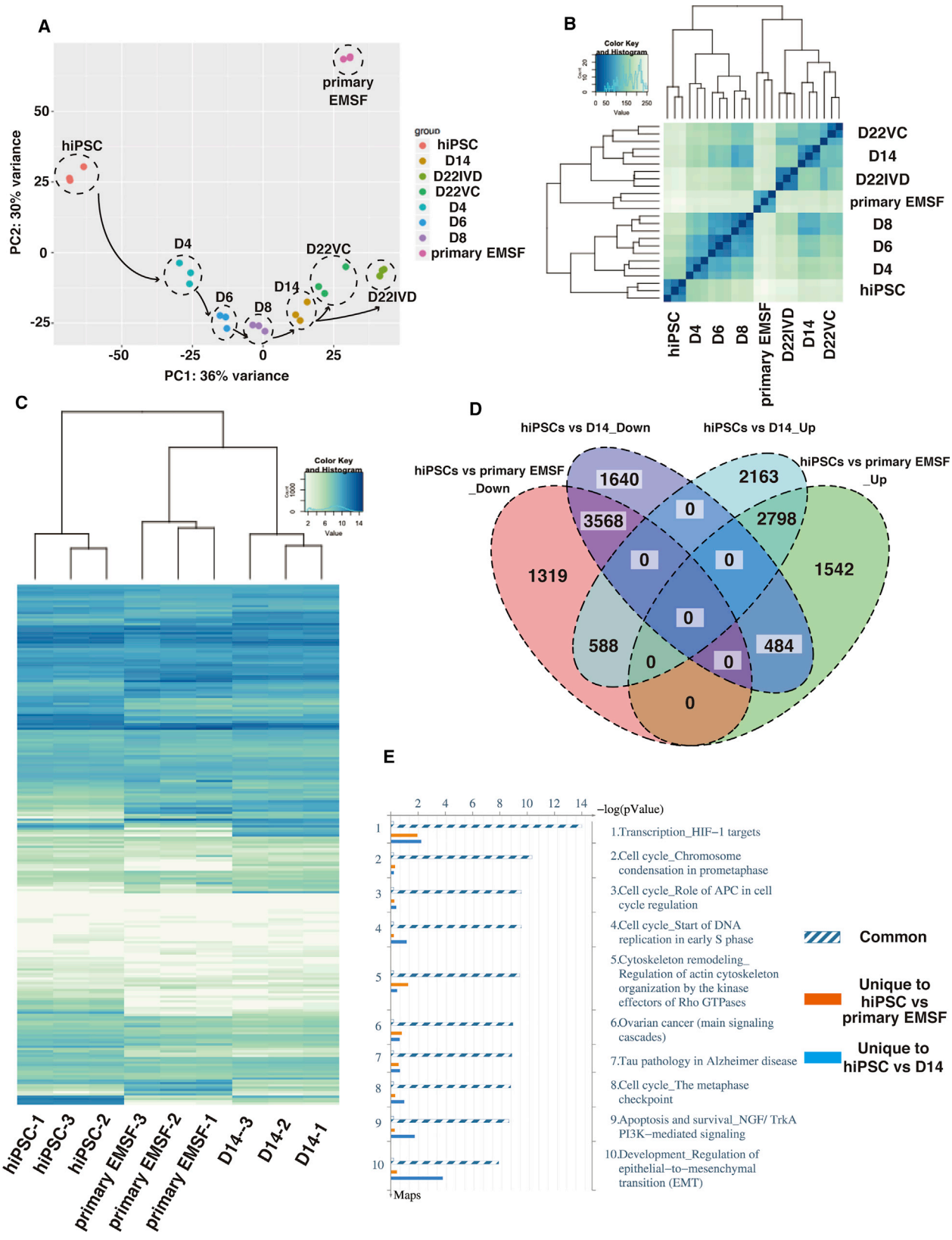

(legend on next page)

of decidualization markers such as *FOXO1*, *HAND2*, *IGFBP1*, and *PRL* (Buzzio et al., 2006) compared with D22 VC (Figure 4C). A similar profile was observed in two independent clones although the upregulation of two of four decidualization markers (*IGFBP1* and *PRL*) observed in primary EMSFs were more prominent compared with D22 EBs (Figures S3B and S3C). ELISA was used to confirm the protein levels of secreted IGFBP1 (Figure 4D). Immunoblot and immunohistochemistry were used to confirm the protein expression of FOXO1 (Figures 4E and 4G). The levels of PRLR, another marker of decidualization (Graubner et al., 2017), was also increased in the D22 IVD versus D22 VC by immunoblot (Figure 4E) and immunohistochemistry (Figure 4G). Quantitative analysis of immunoblot densitometry showed that the protein levels of FOXO1 and PRLR were significantly higher in D22 IVD compared with D22 VC (Figure 4F). The quantitative analysis of immunohistochemistry revealed that the percentages of FOXO1+ cells and PRLR+ cells were significantly higher in D22 IVD compared with D22 VC (51.1% ± 4.2% versus 0%, $p < 0.05$; 54.2% ± 4.2% versus 0%, $p < 0.05$, respectively) (Figure 4H). Furthermore, the mRNA expression of *FKBP5* (Su et al., 2012) and *ZBTB16* (Kommagani et al., 2016), which are direct PGR-target genes, was significantly higher in D22 IVD compared with D22 VC (Figure 4I), showing the progesterone responsiveness of the differentiated cells.

To define a genetic signature of decidualization in the differentiated D22 EBs, we performed RNA sequencing (RNA-seq) to identify differentially expressed genes (DEGs) in D22 IVD relative to D22 VC. Pathway enrichment analysis of the DEGs was performed using MetaCore. The differentially regulated pathways for the DEGs included the cAMP signaling pathway (false discovery rate [FDR] <0.01) (Figure S4A), which is important for the decidual transformation of EMSFs (Brar et al., 1997). See Table S1 for the list of pathways with FDR values obtained in the pathway enrichment analysis. We then compared the D22 DEGs with those from our previously published expression microarray analysis of primary human EMSFs that underwent IVD treatment (Dyson et al., 2014). A total of 1,404 DEGs were upregulated or downregulated similarly in IVD-treated primary EMSFs and hiPSC-derived D22 EMSFs (treated with IVD) compared with respective vehicle controls (adjusted $p < 0.05$) (Figure S3D). Using real-time PCR, we verified major decidualization markers such as FOXO1, HAND2, IGFBP1, which were present among commonly upregulated DEGs in both cell types, supporting our hypothesis that iPSC-derived EMSFs are molecularly quite similar to primary EMSFs (Buzzio et al., 2006). Taken together, we confirmed the decidualization capacity of D14 EBs, and characterized molecular similarities between decidualization of primary EMSFs and iPSC-derived EMSFs, also designated as D14 EBs.

D14 EBs Recapitulate the Molecular Signature of Primary EMSFs

To assess the changes in molecular signatures that occur during the differentiation of hiPSCs in our protocol and how they compare with that in primary EMSFs, we analyzed global gene expression profiles of EBs at each stage (hiPSC, D2.5 EB, D4 EB, D6 EB, D8 EB, D14 EB, D22 VC, and D22 IVD) and of primary EMSFs using RNA-seq. The expression levels of 25,369 genes were measured simultaneously. Unsupervised principal component analysis (PCA) revealed a seamless transition in the transcriptional profiles during differentiation (Figure 5A). Unsupervised hierarchical clustering analysis showed strong correlations between technical replicates in each group and that the D14 EB and D22 EB signatures cluster more closely to primary EMSFs, confirming their resemblance to EMSFs (Figure 5B). Clustered heatmap analysis of 1,434 transcription factor genes revealed greater similarity between the transcriptomes of primary EMSFs and D14 EBs compared with hiPSCs (Figure 5C). See Table S2 for the list of genes used in Figure 5C.

Figure 5. Transcriptome Changes during Differentiation of hiPSCs to EMSFs

(A) Principal component analysis (PCA) of RNA-seq obtained from EBs at each stage of EMSF differentiation from hiPSCs (N = 3 independent experiments).

(B) Hierarchical clustering analysis based on RNA-seq data obtained from EBs at each stage of EMSF differentiation from hiPSCs (N = 3 independent experiments). A total of 25,369 genes analyzed on RNA-seq were used in (A) and (B).

(C) Clustered heatmap analysis comparing the expression of 1,434 transcription factor genes in hiPSCs, D14 EBs, and primary EMSFs (N = 3 independent experiments).

(D) Based on RNA-seq, similar DEGs were identified between D14 EBs and primary EMSFs, relative to hiPSCs (N = 3 independent experiments, FDR adjusted p value <0.05). The Venn diagram shows the total numbers of up- and downregulated genes identified in each comparison. A total of 11,241 and 10,299 DEGs were identified in D14 EBs and primary EMSFs, respectively, compared with hiPSCs (N = 3 independent experiments, FDR adjusted p value <0.05). Since D14 EBs and primary EMSFs share 7,438 DEGs regardless of the direction of the expression, this Venn diagram includes 14,102 (= 11,241 + 10,299 − 7,438) different genes.

(E) Top ten common pathways identified by pathway enrichment analysis performed on the same gene list used in (D) (N = 3 independent experiments, FDR adjusted p value <0.05).

To identify the genes that drive the induction of EMSFs from hiPSCs, we sought common DEGs in primary EMSFs and D14 EBs relative to hiPSCs. A total of 11,241 and 10,299 DEGs were identified in D14 EBs and primary EMSFs, respectively, compared with hiPSCs (adjusted $p < 0.05$). Since D14 EBs and primary EMSFs share 7,438 DEGs regardless of the direction of expression, 14,102 (= 11,241 + 10,299 – 7,438) different sets of genes were used to perform downstream analyses. A total of 6,366 DEGs were similarly upregulated or downregulated in primary EMSFs and D14 EBs compared with hiPSCs (adjusted $p < 0.05$), as demonstrated by the Venn diagram in Figure 5D. Thirty genes (15 upregulated and 15 downregulated genes in D14 and primary EMSFs compared with hiPSCs) with the highest fold changes are listed in the clustered heatmap (Figure S5A). The top 15 downregulated DEGs include pluripotency markers such as *SOX2* and *NANOG*, whereas the top 15 upregulated genes include genes that play crucial roles in endometrial function, such as *WNT2*, *GBP1*, and *POSTN* (Burmenskaya et al., 2017; Kumar et al., 2001; Li et al., 2017). Endometrium-specific transcription factors (*HOXA9*, *HOXA10*, *HOXA11*, and *PGR*) and EMSF markers (*MME*, *COL1A1*, *FN1*, and *VIM*) were present among other common DEGs. Pathway enrichment analysis by MetaCore comparing a total of 14,102 genes included in DEGs in primary EMSFs and D14 EBs relative to hiPSCs showed common enrichment for genes in the cell-cycle regulation pathway (FDR <0.01) and EMT pathway involving transforming growth factor (TGF) and WNT/CTNNB1 pathways (FDR <0.01), indicating that similar pathways are active in primary EMSFs and D14 EBs (Figures 5E and S4B). See Table S3 for the list of pathways with FDR values obtained in the pathway enrichment analysis. Gene ontology (GO) analysis using the same gene list showed common enrichment for "cellular component organization" and "system development" (Figure S5B). See Table S4 for the list of pathways with FDR values obtained in the pathway enrichment analysis. Heatmap analysis based on 133 genes involved in cell-cycle regulation revealed significant similarities between primary EMSFs and D14 EBs compared with hiPSCs (Figure S5C), confirming the result of the pathway enrichment analysis. By contrast, the similarity between primary EMSFs and D14 EBs was relatively weak with regard to the cytoskeleton remodeling pathway or EMT pathway as shown by heatmap analysis of 232 genes involved in these two pathways (Figure S5D). See Table S2 for the list of genes used in Figures S5C and S5D.

To examine the similarity between D14 EBs and eMSCs, we sorted SUSD2-positive eMSCs from freshly isolated primary EMSFs using flow cytometry, and performed RNA-seq. The percentage of SUSD2+ eMSCs among primary EMSFs was 3.6% ± 1.5% (N = 3) (Figure 6A). The mRNA expression of *SUSD2* was significantly higher in the SUSD2-positive population compared with the SUSD2-negative population (Figure 6B), showing the efficient isolation of SUSD2-positive eMSCs. We then performed RNA-seq on the SUSD2-positive population, and compared its global gene expression profile with D14 and primary EMSFs. Unsupervised hierarchical clustering analysis revealed greater similarity between the transcriptomes of primary EMSFs and D14 EBs compared with eMSCs (Figure 6C). These results collectively suggest the proximity of D14 EBs to primary EMSFs, but not eMSCs.

The WNT/CTNNB1 Pathway Is Required for Induction of EMSFs from hiPSCs

Based on the critical effect of CHIR, a CTNNB1 pathway agonist for EMSF induction from hiPSCs in our previous experiments, we hypothesized that the canonical CTNNB1 signaling pathway may play a key role in the differentiation of hiPSCs to EMSFs. Indeed, pathway enrichment analysis showed greater similarity of gene expression in the WNT signaling pathway between primary EMSFs and D14 EBs relative to hiPSCs (Figures 5E and S3B). Since activation of the canonical WNT/CTNNB1 signaling pathway results in the accumulation of CTNNB1 in the nucleus (Nusse, 2005), we performed immunofluorescence of CTNNB1 to determine its cellular localization in EBs. Progressive translocation of CTNNB1 from the plasma membrane to the nucleus was observed at each EB differentiation stage, confirming the activation of the canonical CTNNB1 pathway (Figures 7A and S6).

To determine whether the WNT/CTNNB1 pathway is required for differentiation of hiPSCs to EMSFs, we maintained cultures of D4 EBs (IM-like stage), D6 EBs (CE-like stage), and D8 EBs (MD-like stage) in the absence of CHIR or in the presence of CHIR plus or minus CTNNB1 inhibitors until D6 (CE-like stage), D8 (MD-like stage), and D14 (EMSF-like stage), respectively. Two types of CTNNB1 inhibitors were used. IWP2, an inhibitor of Porcn, was used to block the autocrine secretion of WNT proteins. XAV939 is a Tankyrase inhibitor that stimulates CTNNB1 degradation. We then examined the effects of treatment on expression of *PGR*, *HOXA10*, and *HOXA 11*. Interestingly, withholding CHIR or the addition of CTNNB1 pathway inhibitors (to the regular CHIR-containing cocktail) significantly decreased the expression of *PGR* at every EB stage (Figures 7B–7D), indicating the importance of WNT/CTNNB1 signaling for *PGR* expression at every stage of differentiation of hiPSCs. In contrast, while withholding CHIR or the addition of CTNNB1 pathway inhibitors between D4 and D6 significantly decreased the expression of *HOXA10* and *HOXA11* (Figure 7B), CHIR withdrawal between D6 and D8 had no effect on HOXA gene expression levels (Figure 7C). Furthermore, withholding CHIR

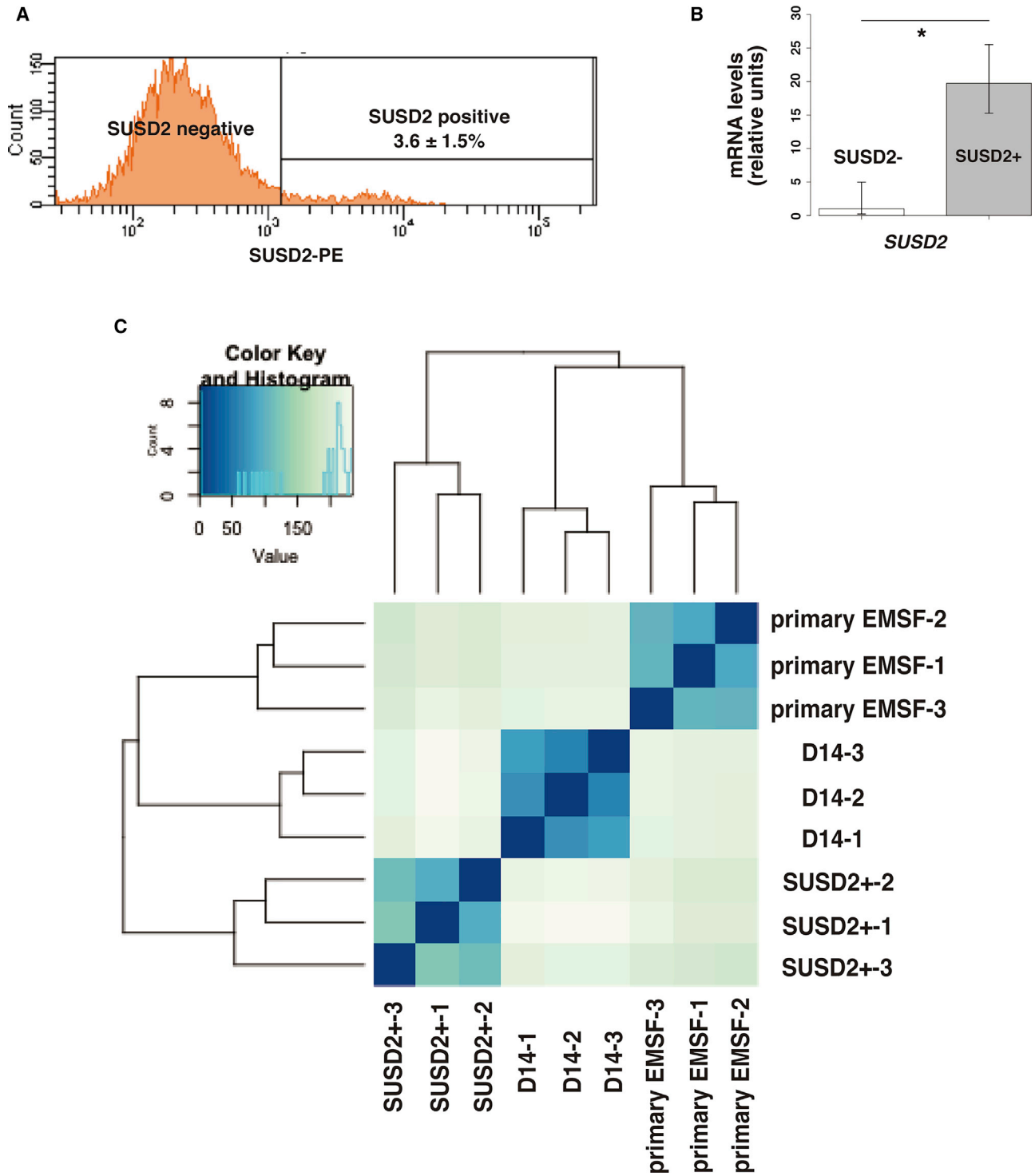

Figure 6. Isolation of SUSD2-Positive Population and Comparison of Its Transcriptome with hiPSC-Derived EMSFs

(A) Representative histogram (N = 3 independent experiments) of the SUSD2-positive population in freshly isolated primary EMSFs.

(B) Quantitative RT-PCR comparing expression of *SUSD2* in the SUSD2-positive and SUSD2-negative population. Error bars represent RQMin and RQMax (N = 3 independent experiments, *p < 0.05, Student's t test).

(C) Hierarchical clustering analysis based on RNA-seq data obtained from D14 EBs, primary EMSFs, and SUSD2+ cells (N = 3 independent experiments). A total of 25,369 genes analyzed on RNA-seq were used in (C).

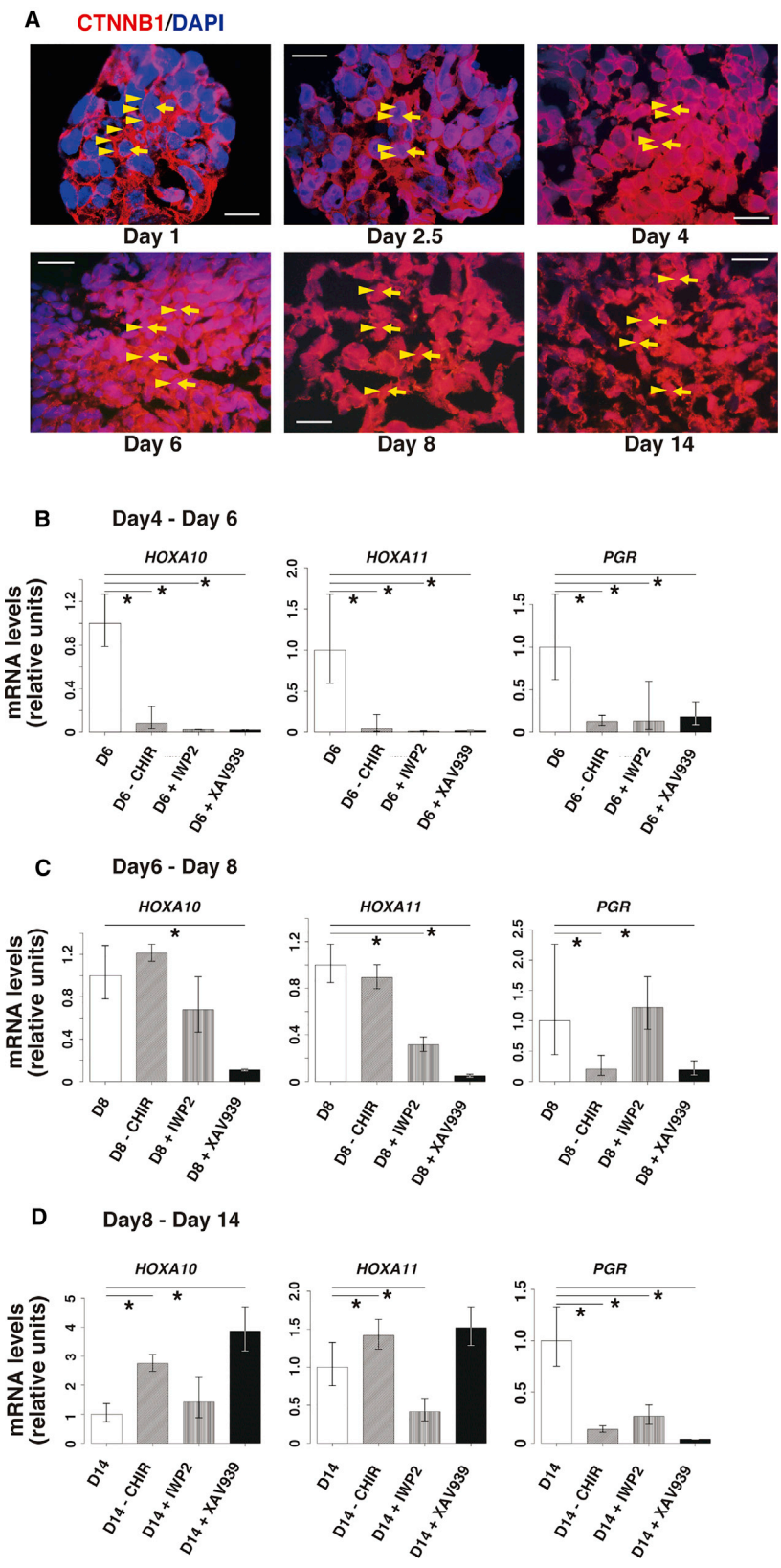

Figure 7. Inhibition of the Canonical WNT/CTNNB1 Pathway

(A) Representative immunofluorescence image of CTNNB1 in hiPSC, D2.5, D4, D6, D8, and D14 EB. Scale bars represent 20 μm. Yellow arrowheads indicate CTNNB1 staining. Yellow arrows indicate DAPI-positive cell nuclei. These images are re-used in Figure S6.

(B–D) Quantitative RT-PCR of EMSF-specific genes *HOXA10*, *HOXA11*, and *PGR* in D6 EBs, D8 EBs, and D14 EBs.

(B) D6 EBs were treated with CHIR, NOGGIN, and PDGF-BB; with NOGGIN and PDGF-BB only; with CHIR, NOGGIN, PDGF-BB, and IWP2; or with CHIR, NOGGIN, PDGF-BB, and XAV939 for 2 days, between D4 and D6. Error bars represent RQMin and RQMax (N = 3 independent experiments except for D6 [N = 9 independent experiments], *p < 0.05, Student's t test).

(C) D8 EB were treated with CHIR and NOGGIN; with NOGGIN only; with CHIR, NOGGIN, and IWP2; or with CHIR, NOGGIN, and XAV939 for 2 days, between D6 and D8. Error bars represent RQMin and RQMax (N = 3 independent experiments except for D8 [N = 9 independent experiments], *p < 0.05, Student's t test).

(D) D14 EBs were treated with 5aza2, CHIR, E_2, FGF9, and PDGF-BB; with 5aza2, E_2, FGF9, and PDGF-BB only; with 5aza2, CHIR, E_2, FGF9, PDGF-BB, and IWP2; or with 5aza2, CHIR, E_2, FGF9, PDGF-BB, and XAV939 for 6 days, between D8 and D14. Error bars represent RQMin and RQMax (N = 3 independent experiments except for D14 [N = 9 independent experiments], *p < 0.05, Student's t test).

or CTNNB1 inhibition between D8 and D14 increased the expression of *HOXA10* and *HOXA11* (Figure 7D). These data suggest that, while the WNT/CTNNB1 pathway is necessary during all stages of endometrial differentiation, it serves diverse functions and seems to be essential for progesterone responsiveness.

DISCUSSION

We defined a protocol to induce the differentiation of EMSFs from hiPSCs under molecularly delineated EB culture conditions. Although the differentiation of human embryonic stem cells and/or hiPSCs to cardiac, hepatic, pancreatic, kidney, or neuronal cell lineages has been widely reported (Batchelder et al., 2009; Chambers et al., 2009; Mae et al., 2013; Song et al., 2009; Zhang et al., 2009a, 2009b), our study represents a demonstration of the successful production of endometrial lineage cells from hiPSCs.

Only a few previous studies have attempted to derive cells of endometrial cell lineage from human embryonic stem cells (Song et al., 2015; Ye et al., 2011; Yu et al., 2015). Ye and colleagues induced mesoderm from a human embryonic stem cell line, co-cultured the mesoderm with murine neonatal endometrial cells, and then transplanted the differentiated cells under the kidney capsule of immunodeficient mice. In the graft, they found epithelium with TUBB (tubulin beta)-positive cilia, which expressed female reproductive tract epithelium markers CK18, CA125, ESR1, and HOXA10 (Ye et al., 2011). Yu and colleagues also demonstrated induction of an endometrium-like cell population, which expressed significantly higher *PRL* after treating a human embryonic stem cell line with a combination of PDGF-BB and WNT5a (Yu et al., 2015). Song et al. (2015) reported differentiation of a human embryonic stem cell line into endometrium-like cells expressing several endometrial markers, using conditioned media from human EMSFs. Of these three previous papers, only Ye et al. (2011) reported the expression of Müllerian duct cell markers during differentiation from mesoderm, whereas changes in gene profiles during the differentiation of the human embryonic stem cells in the studies by Yu et al. (2015) and Song et al. (2015) are not clear. While Yu et al. (2015) did demonstrate possible hormone receptivity of the differentiated endometrium-like cells, since human dermal fibroblast cells also express PRL after IVD (Richards and Hartman, 1996), they were unable to distinguish "endometrium-like cells" from dermal fibroblast cells.

The published protocols to produce Müllerian duct cells from human embryonic stem cells have several limitations. First, these protocols used poorly defined components, such as conditioned medium obtained from endometrial cell culture (Song et al., 2015) and co-culture with endometrium obtained from newborn mice (Ye et al., 2011), which would not be suitable for clinical applications. Second, since human embryonic stem cells are established from the inner cell mass of an embryo, the tissues derived from these cells cannot be transplanted to patients without an immune rejection.

Although hiPSCs are more difficult to differentiate than human embryonic stem cells (Kuzmenkin et al., 2009), hiPSCs present fewer ethical problems than human embryonic stem cells and are able to produce histocompatible tissues for autologous transplantation (Kondo et al., 2017). Thus, hiPSC research is expected to lead to regenerative therapies for various disorders, possibly including uterine factor infertility and endometriosis.

Here, we attempted to reproduce each stage of EMSF development, confirming the lineage of the differentiated cells at each step based on the presence and absence of cell-specific marker genes. We used an established protocol for the first step, IM induction, using a previously established protocol from Lam et al. (2014). We detected robust upregulation of LHX1 and PAX2 via PS differentiation using sequential treatment with CHIR, FGF2, and RA, consistent with the findings of Lam et al. (2014). We then used a WNT/CTNNB1 pathway agonist along with other chemical cocktails following the published findings that suggest a critical role of the WNT/CTNNB1 pathway in the differentiation of Müllerian tissues (Deutscher and Hung-Chang Yao, 2007; Stewart et al., 2013). With each step, our protocol produced EBs with gene expression profiles similar to CE, MD, and endometrial cells.

Importantly, we also demonstrated that the transcriptomes of the hiPSC-derived EMSFs and primary EMSFs were similar in the hierarchical analysis and heatmap analysis. Temporal changes in transcription factor genes are critical for development, as they turn on or off the appropriate genes in response to various growth factors to regulate changes in cell morphology and function that determine cell fate and differentiation (Lobe, 1992). For example, the HOX transcription factor family is important for proper body pattern formation (Moens and Selleri, 2006). A characteristic spatial distribution of HOXA9-13 is seen throughout the MD of vertebrates (Goodman, 2002). HOXA9 is expressed in the oviduct, HOXA10 is expressed in the uterus, HOXA11 is found in the lower uterus and cervix, and HOXA13 is seen in the ectocervix and upper vagina (Du and Taylor, 2015). Interestingly, HOXA9, 10, and 11, but not 13, were similarly regulated in D14 EBs and EMSFs, but distinct from hiPSCs.

The PCA partly supported the similarity of hiPSC-derived EMSFs and primary EMSFs: on the PC1 axis, the transcriptome distance between primary EMSFs and EBs became progressively closer during the differentiation process. To

assess the gene signature that drives the induction of EMSFs, we identified 30 common DEGs with the highest fold changes in D14 and primary EMSFs relative to hiPSCs. Although the PCA was generated from the whole transcriptome, it is inferable that these DEGs significantly contributed to the transition observed in PCA.

Pathway enrichment analysis further revealed that EMSFs and D14 EBs show common enrichment for genes in the cell-cycle regulation pathway, EMT pathway, and cytoskeleton remodeling pathway that involves TGF and WNT, relative to hiPSCs. However, while a heatmap of cell-cycle regulation gene expression clearly demonstrated the similarity between D14 EBs and primary EMSFs, a heatmap of EMT pathway and cytoskeleton pathway genes showed only weak similarity between D14 EBs and primary EMSFs. This discrepancy between pathway enrichment analysis and heatmap gene expression may be explained by the difference in fold change between primary EMSFs and D14 EBs relative to hiPSCs, as pathway enrichment analysis only relies on the direction of gene regulation (i.e., upregulation or downregulation).

Hormone responsiveness is a defining characteristic of the endometrial stroma. In the secretory phase of the human menstrual cycle, progesterone exerts its action on EMSFs by binding to PGR, a member of the steroid hormone receptor superfamily of ligand-activated transcription factors, promoting differentiation of the cells in a process termed decidualization (Gellersen and Brosens, 2003). When hiPSC-derived EBs were treated with estrogen, progestin, and a cAMP analog, they underwent decidualization, and the resulting D22 EBs had a similar transcriptome expression pattern as primary EMSFs, with approximately 20%–30% of all DEGs similarly up- or downregulated in response to IVD treatment. The upregulation of direct PGR-target genes in response to the hormone treatment further supported the active PGR signaling pathway in the differentiated cells.

Our method of using CHIR to induce differentiation into Müllerian lineage is consistent with the important role of WNT/CTNNB1 signaling during embryonic MD development (Deutscher and Hung-Chang Yao, 2007; Stewart et al., 2013). Indeed, the addition of CTNNB1 inhibitors led to downregulation of *PGR*, suggesting a critical relationship between the canonical WNT/CTNNB1 signaling pathway and *PGR* expression, at least in the developing MD. Further study is needed to clarify the interaction between these signaling cascades.

hiPSC-derived EMSFs cultured as EBs displayed many specific characteristics of primary EMSFs such as expression of the critical genes including PGR, HOXA11, PRL, and IGFBP1. There were, however, some quantitative differences between the two cell types. For example, progesterone fold induction of PRL or IGFBP1 was lower in hiPSC-derived EMSFs. Moreover, the expression levels of general fibroblast markers such as VIM were lower in hiPSC-derived EMSFs compared with primary EMSFs. We anticipate that further optimization of the current protocol and experimental model will improve these aspects in the future.

Further study is also needed to generate endometrial epithelial cells from hiPSCs. Whereas EMSFs are relatively easy to grow on a 2D culture dish, endometrial epithelial cells are more difficult to maintain. Recently, Turco et al. (2017) reported a method for long-term, hormone-responsive organoid culture of human endometrium in a chemically defined medium. Their approach may help elucidate the distinct physiology of endometrial epithelial cells and lead to a new protocol to generate endometrial epithelial cells from hiPSCs in the future.

With regard to the potential clinical applications of our work, we envision that the protocol to differentiate EMSFs from hiPSCs will one day be amenable to cell replacement therapy for endometrial diseases such as endometriosis or early-stage low-grade endometrial cancer, in which abnormal EMSFs contribute to pathogenesis (Janzen et al., 2013; Kim et al., 2013). Cell replacement therapy may also be effective for the treatment of uterine factor infertility, such as Asherman syndrome (intrauterine adhesions). Future studies will explore the use of natural or synthetic scaffolds of differentiated iPSC-derived EMSFs for transplantation. In fact, endometrium-like tissues were successfully regenerated from decellularized rat uterine matrix reseeded with rat uterine cells (Miyazaki and Maruyama, 2014). This technology may become a component of a novel therapeutic strategy for treating uterine agenesis. Also, further work is needed to elucidate the precise molecular pathways within the WNT/CTNNB1 signaling cascade for the regulation of *PGR* during differentiation of stem cells, which can lead to a novel molecular therapy for a variety of endometrial diseases since abnormal responses to progesterone play key roles in the pathogenesis of such disorders.

In conclusion, defined sequential incubation with a CTNNB1 activator and a number of other specific hormones induces differentiation of hiPSCs into EBs with similar gene expression patterns as EMSFs; these cells are capable of decidualization in response to a time-honored hormonal stimulation. We also demonstrated that the canonical CTNNB1 signaling pathway is essential for the expression of *PGR*, the key steroid hormone receptor and master regulator of the most important function of the endometrium, i.e., implantation of an embryo (Kim et al., 2013). The establishment of a protocol for differentiating hiPSCs into cells of the endometrial stromal cell lineage will have implications for cell-based therapies and bioengineering of endometrial tissue for the treatment of various endometrial diseases such as endometriosis, early-stage endometrial cancer, and uterine factor infertility.

EXPERIMENTAL PROCEDURES

Contact for Reagent and Resource Sharing

Further information and requests for resources and reagents should be directed to and will be fulfilled by the lead contact, Serdar E. Bulun (s-bulun@northwestern.edu).

Experimental Model and Subject Details

Ethics Statement

The acquisition of human tissue for this study was approved by the Northwestern Institutional Review Board for Human Research (1375–005). Written informed consent from each subject was obtained before surgery.

Method Details

hiPSC Culture

Two hiPSC lines (clone 1, ACS-1028; clone 2, ACS-1030) were purchased from American Type Culture Collection (Manassas, VA). Clones 1 and 2 were derived from bone marrow CD34+ cells obtained from a healthy African American female donor and a white female donor, respectively, with Sendai viral expression of OCT4, SOX2, KLF4, and MYC genes. The cells were routinely cultured on feeder layers of mitomycin C-treated mouse embryonic fibroblast feeder cells (Applied StemCells, Milpitas, CA), seeded on gelatin-coated dishes (MilliporeSigma, Burlington, MA), in hiPSC maintenance medium (DMEM/F12 + 20% KnockOut Serum Replacement + 1 mM nonessential amino acids + 2 mM GlutaMAX + 0.55 mM 2-mercaptoethanol [all from Thermo Fisher Scientific, Carlsbad, CA]) supplemented with 10 ng/mL recombinant human FGF2 (PeproTech, Rocky Hill, NJ) (passages 9–13). Cell plastics were from TPP (St. Louis, MO). Cultures were passaged using calcium-/magnesium-free PBS (Thermo Fisher Scientific) supplemented with 0.5 mM EDTA (VWR, Radnor, PA) and 30.8 mM NaCl (MilliporeSigma) at a 1:4 split ratio every 3–5 days.

See Supplemental Experimental Procedures for method details.

ACCESSION NUMBERS

RNA-seq data have been deposited in the ArrayExpress database at EMBL-EBI (www.ebi.ac.uk/arrayexpress) under accession number ArrayExpress: E-MTAB-7292.

SUPPLEMENTAL INFORMATION

Supplemental Information includes Supplemental Experimental Procedures, six figures, and seven tables and can be found with this article online at https://doi.org/10.1016/j.stemcr.2018.10.002.

AUTHOR CONTRIBUTIONS

K.M., T.M., and S.E.B. conceived and designed the experiments. K.M., M.T.D., J.S.C., Y.F., B.D.Y., and S.E.B. performed the experiments. K.M., M.T.D., and S.E.B. analyzed the data. K.M., M.T.D., J.S.C., and S.E.B. contributed reagents/materials/analysis tools. K.M. and S.E.B. wrote the manuscript. K.M., M.T.D., T.M., and S.E.B. reviewed the manuscript.

ACKNOWLEDGMENTS

The authors thank Dr. Masashi Toyoda for his valuable advice on hiPSC culture. The authors thank Dr. Matthew Schipma for his technical support for RNA-seq data analysis. The authors thank Dr. Demirkan Gursel for his technical support for immunostaining. This study was supported by funding from NIH grant R37-HD36891 (S.E.B.) and R03-HD082558 (M.T.D.), Grant-in-Aid for Scientific Research (Young Scientists B) (K.M.), the Uehara Memorial Foundation (K.M.), and the Kanzawa Medical Research Foundation (K.M.).

Received: June 13, 2018
Revised: October 1, 2018
Accepted: October 2, 2018
Published: November 1, 2018

REFERENCES

Akamatsu, T., Arai, Y., Kosugi, I., Kawasaki, H., Meguro, S., Sakao, M., Shibata, K., Suda, T., Chida, K., and Iwashita, T. (2013). Direct isolation of myofibroblasts and fibroblasts from bleomycin-injured lungs reveals their functional similarities and differences. Fibrogenesis Tissue Repair *6*, 15.

Arango, N.A., and Donahoe, P.K. (2008). Sex differentiation in mouse and man and subsequent development of the female reproductive organs. In StemBook (Harvard Stem Cell Institute). https://www.ncbi.nlm.nih.gov/books/NBK47454/.

Araoka, T., Mae, S., Kurose, Y., Uesugi, M., Ohta, A., Yamanaka, S., and Osafune, K. (2014). Efficient and rapid induction of human iPSCs/ESCs into nephrogenic intermediate mesoderm using small molecule-based differentiation methods. PLoS One *9*, e84881.

Banerjee, S., and Bacanamwo, M. (2010). DNA methyltransferase inhibition induces mouse embryonic stem cell differentiation into endothelial cells. Exp. Cell Res. *316*, 172–180.

Batchelder, C.A., Lee, C.C., Matsell, D.G., Yoder, M.C., and Tarantal, A.F. (2009). Renal ontogeny in the rhesus monkey (*Macaca mulatta*) and directed differentiation of human embryonic stem cells towards kidney precursors. Differentiation *78*, 45–56.

Benson, G.V., Lim, H., Paria, B.C., Satokata, I., Dey, S.K., and Maas, R.L. (1996). Mechanisms of reduced fertility in Hoxa-10 mutant mice: uterine homeosis and loss of maternal Hoxa-10 expression. Development *122*, 2687–2696.

Brar, A.K., Frank, G.R., Kessler, C.A., Cedars, M.I., and Handwerger, S. (1997). Progesterone-dependent decidualization of the human endometrium is mediated by cAMP. Endocrine *6*, 301–307.

Bulun, S.E. (2009). Endometriosis. N. Engl. J. Med. *360*, 268–279.

Burmenskaya, O.V., Bozhenko, V.K., Smolnikova, V.Y., Kalinina, E.A., Korneeva, I.E., Donnikov, A.E., Beyk capital Ie, C., Naumov, V.A., Aleksandrova, N.V., Borovikov, P.I., et al. (2017). Transcription profile analysis of the endometrium revealed molecular markers of the personalized 'window of implantation' during in vitro fertilization. Gynecol. Endocrinol. *33*, 22–27.

Busch, S., Andersson, D., Bom, E., Walsh, C., Stahlberg, A., and Landberg, G. (2017). Cellular organization and molecular

differentiation model of breast cancer-associated fibroblasts. Mol. Cancer *16*, 73.

Buzzio, O.L., Lu, Z., Miller, C.D., Unterman, T.G., and Kim, J.J. (2006). FOXO1A differentially regulates genes of decidualization. Endocrinology *147*, 3870–3876.

Chambers, S.M., Fasano, C.A., Papapetrou, E.P., Tomishima, M., Sadelain, M., and Studer, L. (2009). Highly efficient neural conversion of human ES and iPS cells by dual inhibition of SMAD signaling. Nat. Biotechnol. *27*, 275–280.

Chan, R.W., Schwab, K.E., and Gargett, C.E. (2004). Clonogenicity of human endometrial epithelial and stromal cells. Biol. Reprod. *70*, 1738–1750.

Cheng, F., Shen, Y., Mohanasundaram, P., Lindstrom, M., Ivaska, J., Ny, T., and Eriksson, J.E. (2016). Vimentin coordinates fibroblast proliferation and keratinocyte differentiation in wound healing via TGF-beta-Slug signaling. Proc. Natl. Acad. Sci. U S A *113*, E4320–E4327.

D'Amour, K.A., Agulnick, A.D., Eliazer, S., Kelly, O.G., Kroon, E., and Baetge, E.E. (2005). Efficient differentiation of human embryonic stem cells to definitive endoderm. Nat. Biotechnol. *23*, 1534–1541.

Daftary, G.S., and Taylor, H.S. (2004). EMX2 gene expression in the female reproductive tract and aberrant expression in the endometrium of patients with endometriosis. J. Clin. Endocrinol. Metab. *89*, 2390–2396.

Daley, G.Q. (2012). The promise and perils of stem cell therapeutics. Cell Stem Cell *10*, 740–749.

Davidson, B.P., and Tam, P.P. (2000). The node of the mouse embryo. Curr. Biol. *10*, R617–R619.

Deutscher, E., and Hung-Chang Yao, H. (2007). Essential roles of mesenchyme-derived beta-catenin in mouse Mullerian duct morphogenesis. Dev. Biol. *307*, 227–236.

Di Carlo, F., Racca, S., Gallo, E., Conti, G., Russo, A., Mondo, F., and Francalanci, S. (1985). Estrogen and progesterone receptors in the human vagina. J. Endocrinol. Invest. *8*, 131–134.

Du, H., and Taylor, H.S. (2015). The role of hox genes in female reproductive tract development, adult function, and fertility. Cold Spring Harb. Perspect. Med. *6*, a023002.

Dyson, M.T., Roqueiro, D., Monsivais, D., Ercan, C.M., Pavone, M.E., Brooks, D.C., Kakinuma, T., Ono, M., Jafari, N., Dai, Y., et al. (2014). Genome-wide DNA methylation analysis predicts an epigenetic switch for GATA factor expression in endometriosis. PLoS Genet. *10*, e1004158.

Edson, M.A., Nagaraja, A.K., and Matzuk, M.M. (2009). The mammalian ovary from genesis to revelation. Endocr. Rev. *30*, 624–712.

Familari, M. (2006). Characteristics of the endoderm: embryonic and extraembryonic in mouse. ScientificWorldJournal *6*, 1815–1827.

Gadue, P., Huber, T.L., Paddison, P.J., and Keller, G.M. (2006). Wnt and TGF-beta signaling are required for the induction of an in vitro model of primitive streak formation using embryonic stem cells. Proc. Natl. Acad. Sci. U S A *103*, 16806–16811.

Gao, L.R., Li, S., Zhang, J., Liang, C., Chen, E.N., Zhang, S.Y., Chuai, M., Bao, Y.P., Wang, G., and Yang, X. (2016). Excess imidacloprid exposure causes the heart tube malformation of chick embryos. J. Agric. Food Chem. *64*, 9078–9088.

Gellersen, B., and Brosens, J. (2003). Cyclic AMP and progesterone receptor cross-talk in human endometrium: a decidualizing affair. J. Endocrinol. *178*, 357–372.

Gendron, R.L., Paradis, H., Hsieh-Li, H.M., Lee, D.W., Potter, S.S., and Markoff, E. (1997). Abnormal uterine stromal and glandular function associated with maternal reproductive defects in Hoxa-11 null mice. Biol. Reprod. *56*, 1097–1105.

Giudice, L.C. (2010). Clinical practice. Endometriosis. N. Engl. J. Med. *362*, 2389–2398.

Goodman, F.R. (2002). Limb malformations and the human HOX genes. Am. J. Med. Genet. *112*, 256–265.

Graubner, F.R., Reichler, I.M., Rahman, N.A., Payan-Carreira, R., Boos, A., and Kowalewski, M.P. (2017). Decidualization of the canine uterus: from early until late gestational in vivo morphological observations, and functional characterization of immortalized canine uterine stromal cell lines. Reprod. Domest. Anim. *52*(Suppl 2), 137–147.

Guioli, S., Sekido, R., and Lovell-Badge, R. (2007). The origin of the Mullerian duct in chick and mouse. Dev. Biol. *302*, 389–398.

Han, D.W., Greber, B., Wu, G., Tapia, N., Arauzo-Bravo, M.J., Ko, K., Bernemann, C., Stehling, M., and Scholer, H.R. (2011). Direct reprogramming of fibroblasts into epiblast stem cells. Nat. Cell Biol. *13*, 66–71.

Hashimoto, R. (2003). Development of the human Mullerian duct in the sexually undifferentiated stage. Anat. Rec. A Discov. Mol. Cell. Evol. Biol. *272*, 514–519.

Horrillo, A., Pezzolla, D., Fraga, M.F., Aguilera, Y., Salguero-Aranda, C., Tejedo, J.R., Martin, F., Bedoya, F.J., Soria, B., and Hmadcha, A. (2013). Zebularine regulates early stages of mESC differentiation: effect on cardiac commitment. Cell Death Dis. *4*, e570.

Imai, K., Maeda, M., Fujiwara, H., Okamoto, N., Kariya, M., Emi, N., Takakura, K., Kanzaki, H., and Mori, T. (1992). Human endometrial stromal cells and decidual cells express cluster of differentiation (CD) 13 antigen/aminopeptidase N and CD10 antigen/neutral endopeptidase. Biol. Reprod. *46*, 328–334.

Jameson, S.A., Natarajan, A., Cool, J., DeFalco, T., Maatouk, D.M., Mork, L., Munger, S.C., and Capel, B. (2012). Temporal transcriptional profiling of somatic and germ cells reveals biased lineage priming of sexual fate in the fetal mouse gonad. PLoS Genet. *8*, e1002575.

Janzen, D.M., Rosales, M.A., Paik, D.Y., Lee, D.S., Smith, D.A., Witte, O.N., Iruela-Arispe, M.L., and Memarzadeh, S. (2013). Progesterone receptor signaling in the microenvironment of endometrial cancer influences its response to hormonal therapy. Cancer Res. *73*, 4697–4710.

Kim, J.J., Kurita, T., and Bulun, S.E. (2013). Progesterone action in endometrial cancer, endometriosis, uterine fibroids, and breast cancer. Endocr. Rev. *34*, 130–162.

Kobayashi, A., and Behringer, R.R. (2003). Developmental genetics of the female reproductive tract in mammals. Nat. Rev. Genet. *4*, 969–980.

Kommagani, R., Szwarc, M.M., Vasquez, Y.M., Peavey, M.C., Mazur, E.C., Gibbons, W.E., Lanz, R.B., DeMayo, F.J., and Lydon, J.P. (2016). The promyelocytic leukemia zinc finger transcription factor is critical for human endometrial stromal cell decidualization. PLoS Genet. *12*, e1005937.

Kondo, Y., Toyoda, T., Inagaki, N., and Osafune, K. (2017). iPSC technology-based regenerative therapy for diabetes. J. Diabetes Invest. *9*, 234–243.

Kumar, S., Li, Q., Dua, A., Ying, Y.K., Bagchi, M.K., and Bagchi, I.C. (2001). Messenger ribonucleic acid encoding interferon-inducible guanylate binding protein 1 is induced in human endometrium within the putative window of implantation. J. Clin. Endocrinol. Metab. *86*, 2420–2427.

Kuzmenkin, A., Liang, H., Xu, G., Pfannkuche, K., Eichhorn, H., Fatima, A., Luo, H., Saric, T., Wernig, M., Jaenisch, R., et al. (2009). Functional characterization of cardiomyocytes derived from murine induced pluripotent stem cells in vitro. FASEB J. *23*, 4168–4180.

Lam, A.Q., Freedman, B.S., Morizane, R., Lerou, P.H., Valerius, M.T., and Bonventre, J.V. (2014). Rapid and efficient differentiation of human pluripotent stem cells into intermediate mesoderm that forms tubules expressing kidney proximal tubular markers. J. Am. Soc. Nephrol. *25*, 1211–1225.

Li, N., Li, S., Wang, Y., Wang, J., Wang, K., Liu, X., Li, Y., and Liu, J. (2017). Decreased expression of WNT2 in villi of unexplained recurrent spontaneous abortion patients may cause trophoblast cell dysfunction via downregulated Wnt/beta-catenin signaling pathway. Cell Biol. Int. *41*, 898–907.

Little, M., Georgas, K., Pennisi, D., and Wilkinson, L. (2010). Kidney development: two tales of tubulogenesis. Curr. Top. Dev. Biol. *90*, 193–229.

Lobe, C.G. (1992). Transcription factors and mammalian development. Curr. Top. Dev. Biol. *27*, 351–383.

Mae, S., Shono, A., Shiota, F., Yasuno, T., Kajiwara, M., Gotoda-Nishimura, N., Arai, S., Sato-Otubo, A., Toyoda, T., Takahashi, K., et al. (2013). Monitoring and robust induction of nephrogenic intermediate mesoderm from human pluripotent stem cells. Nat. Commun. *4*, 1367.

Mahmood, T.A., and Templeton, A. (1991). Prevalence and genesis of endometriosis. Hum. Reprod. *6*, 544–549.

Maruyama, T., and Yoshimura, Y. (2008). Molecular and cellular mechanisms for differentiation and regeneration of the uterine endometrium. Endocr. J. *55*, 795–810.

Maruyama, T., Masuda, H., Ono, M., Kajitani, T., and Yoshimura, Y. (2010). Human uterine stem/progenitor cells: their possible role in uterine physiology and pathology. Reproduction *140*, 11–22.

Masuda, H., Anwar, S.S., Buhring, H.J., Rao, J.R., and Gargett, C.E. (2012). A novel marker of human endometrial mesenchymal stem-like cells. Cell Transplant. *21*, 2201–2214.

Miyazaki, K., and Maruyama, T. (2014). Partial regeneration and reconstruction of the rat uterus through recellularization of a decellularized uterine matrix. Biomaterials *35*, 8791–8800.

Miyazaki, K., Maruyama, T., Masuda, H., Yamasaki, A., Uchida, S., Oda, H., Uchida, H., and Yoshimura, Y. (2012). Stem cell-like differentiation potentials of endometrial side population cells as revealed by a newly developed in vivo endometrial stem cell assay. PLoS One *7*, e50749.

Moens, C.B., and Selleri, L. (2006). Hox cofactors in vertebrate development. Dev. Biol. *291*, 193–206.

Morizane, R., Lam, A.Q., Freedman, B.S., Kishi, S., Valerius, M.T., and Bonventre, J.V. (2015). Nephron organoids derived from human pluripotent stem cells model kidney development and injury. Nat. Biotechnol. *33*, 1193–1200.

Mote, P.A., Balleine, R.L., McGowan, E.M., and Clarke, C.L. (1999). Colocalization of progesterone receptors A and B by dual immunofluorescent histochemistry in human endometrium during the menstrual cycle. J. Clin. Endocrinol. Metab. *84*, 2963–2971.

Mugford, J.W., Sipila, P., McMahon, J.A., and McMahon, A.P. (2008). Osr1 expression demarcates a multi-potent population of intermediate mesoderm that undergoes progressive restriction to an Osr1-dependent nephron progenitor compartment within the mammalian kidney. Dev. Biol. *324*, 88–98.

Mutlu, L., Hufnagel, D., and Taylor, H.S. (2015). The endometrium as a source of mesenchymal stem cells for regenerative medicine. Biol. Reprod. *92*, 138.

Nusse, R. (2005). Wnt signaling in disease and in development. Cell Res. *15*, 28–32.

Palpant, N.J., Pabon, L., Friedman, C.E., Roberts, M., Hadland, B., Zaunbrecher, R.J., Bernstein, I., Zheng, Y., and Murry, C.E. (2017). Generating high-purity cardiac and endothelial derivatives from patterned mesoderm using human pluripotent stem cells. Nat. Protoc. *12*, 15–31.

Peterson, A.J., Hunter, J.T., Welch, R.A., and Fairclough, R.J. (1975). Oestrogens in bovine fetal and maternal plasma near term. J. Reprod. Fertil. *43*, 179–181.

Ramkumar, N., and Anderson, K.V. (2011). SnapShot: mouse primitive streak. Cell *146*, 488–488.e2.

Richards, R.G., and Hartman, S.M. (1996). Human dermal fibroblast cells express prolactin in vitro. J. Invest. Dermatol. *106*, 1250–1255.

Salih, S.M., and Taylor, H.S. (2004). HOXA10 gene expression in human fallopian tube and ectopic pregnancy. Am. J. Obstet. Gynecol. *190*, 1404–1406.

Siegel, R., Naishadham, D., and Jemal, A. (2013). Cancer statistics, 2013. CA Cancer J. Clin. *63*, 11–30.

Song, Z., Cai, J., Liu, Y., Zhao, D., Yong, J., Duo, S., Song, X., Guo, Y., Zhao, Y., Qin, H., et al. (2009). Efficient generation of hepatocyte-like cells from human induced pluripotent stem cells. Cell Res. *19*, 1233–1242.

Song, T., Zhao, X., Sun, H., Li, X., Lin, N., Ding, L., Dai, J., and Hu, Y. (2015). Regeneration of uterine horns in rats using collagen scaffolds loaded with human embryonic stem cell-derived endometrium-like cells. Tissue Eng. Part A *21*, 353–361.

Stewart, C.A., Wang, Y., Bonilla-Claudio, M., Martin, J.F., Gonzalez, G., Taketo, M.M., and Behringer, R.R. (2013). CTNNB1 in mesenchyme regulates epithelial cell differentiation during Mullerian duct and postnatal uterine development. Mol. Endocrinol. *27*, 1442–1454.

Su, S., Blackwelder, A.J., Grossman, G., Minges, J.T., Yuan, L., Young, S.L., and Wilson, E.M. (2012). Primate-specific melanoma antigen-A11 regulates isoform-specific human progesterone receptor-B transactivation. J. Biol. Chem. *287*, 34809–34824.

Takahashi, K., Tanabe, K., Ohnuki, M., Narita, M., Ichisaka, T., Tomoda, K., and Yamanaka, S. (2007). Induction of pluripotent stem cells from adult human fibroblasts by defined factors. Cell *131*, 861–872.

Tsai, S.J., Wu, M.H., Chen, H.M., Chuang, P.C., and Wing, L.Y. (2002). Fibroblast growth factor-9 is an endometrial stromal growth factor. Endocrinology *143*, 2715–2721.

Turco, M.Y., Gardner, L., Hughes, J., Cindrova-Davies, T., Gomez, M.J., Farrell, L., Hollinshead, M., Marsh, S.G.E., Brosens, J.J., Critchley, H.O., et al. (2017). Long-term, hormone-responsive organoid cultures of human endometrium in a chemically defined medium. Nat. Cell Biol. *19*, 568–577.

Warren, L., Manos, P.D., Ahfeldt, T., Loh, Y.H., Li, H., Lau, F., Ebina, W., Mandal, P.K., Smith, Z.D., Meissner, A., et al. (2010). Highly efficient reprogramming to pluripotency and directed differentiation of human cells with synthetic modified mRNA. Cell Stem Cell *7*, 618–630.

Wilhelm, D., Palmer, S., and Koopman, P. (2007). Sex determination and gonadal development in mammals. Physiol. Rev. *87*, 1–28.

Ye, L., Mayberry, R., Lo, C.Y., Britt, K.L., Stanley, E.G., Elefanty, A.G., and Gargett, C.E. (2011). Generation of human female reproductive tract epithelium from human embryonic stem cells. PLoS One *6*, e21136.

Young, P.E., Baumhueter, S., and Lasky, L.A. (1995). The sialomucin CD34 is expressed on hematopoietic cells and blood vessels during murine development. Blood *85*, 96–105.

Yu, J., Vodyanik, M.A., Smuga-Otto, K., Antosiewicz-Bourget, J., Frane, J.L., Tian, S., Nie, J., Jonsdottir, G.A., Ruotti, V., Stewart, R., et al. (2007). Induced pluripotent stem cell lines derived from human somatic cells. Science *318*, 1917–1920.

Yu, W.Z., Chen, X.M., Niu, W.B., Wang, F., Sun, B., and Sun, Y.P. (2015). Role of Wnt5a in the differentiation of human embryonic stem cells into endometrium-like cells. Int. J. Clin. Exp. Pathol. *8*, 5478–5484.

Zhang, D., Jiang, W., Liu, M., Sui, X., Yin, X., Chen, S., Shi, Y., and Deng, H. (2009a). Highly efficient differentiation of human ES cells and iPS cells into mature pancreatic insulin-producing cells. Cell Res. *19*, 429–438.

Zhang, J., Wilson, G.F., Soerens, A.G., Koonce, C.H., Yu, J., Palecek, S.P., Thomson, J.A., and Kamp, T.J. (2009b). Functional cardiomyocytes derived from human induced pluripotent stem cells. Circ. Res. *104*, e30–e41.

Zimmerlin, L., Park, T.S., and Zambidis, E.T. (2017). Capturing human naive pluripotency in the embryo and in the dish. Stem Cells Dev. *26*, 1141–1161.

Stem Cell Reports, Volume *11*

Supplemental Information

Generation of Progesterone-Responsive Endometrial Stromal Fibroblasts from Human Induced Pluripotent Stem Cells: Role of the WNT/CTNNB1 Pathway

Kaoru Miyazaki, Matthew T. Dyson, John S. Coon V, Yuichi Furukawa, Bahar D. Yilmaz, Tetsuo Maruyama, and Serdar E. Bulun

Supplemental Figure 1

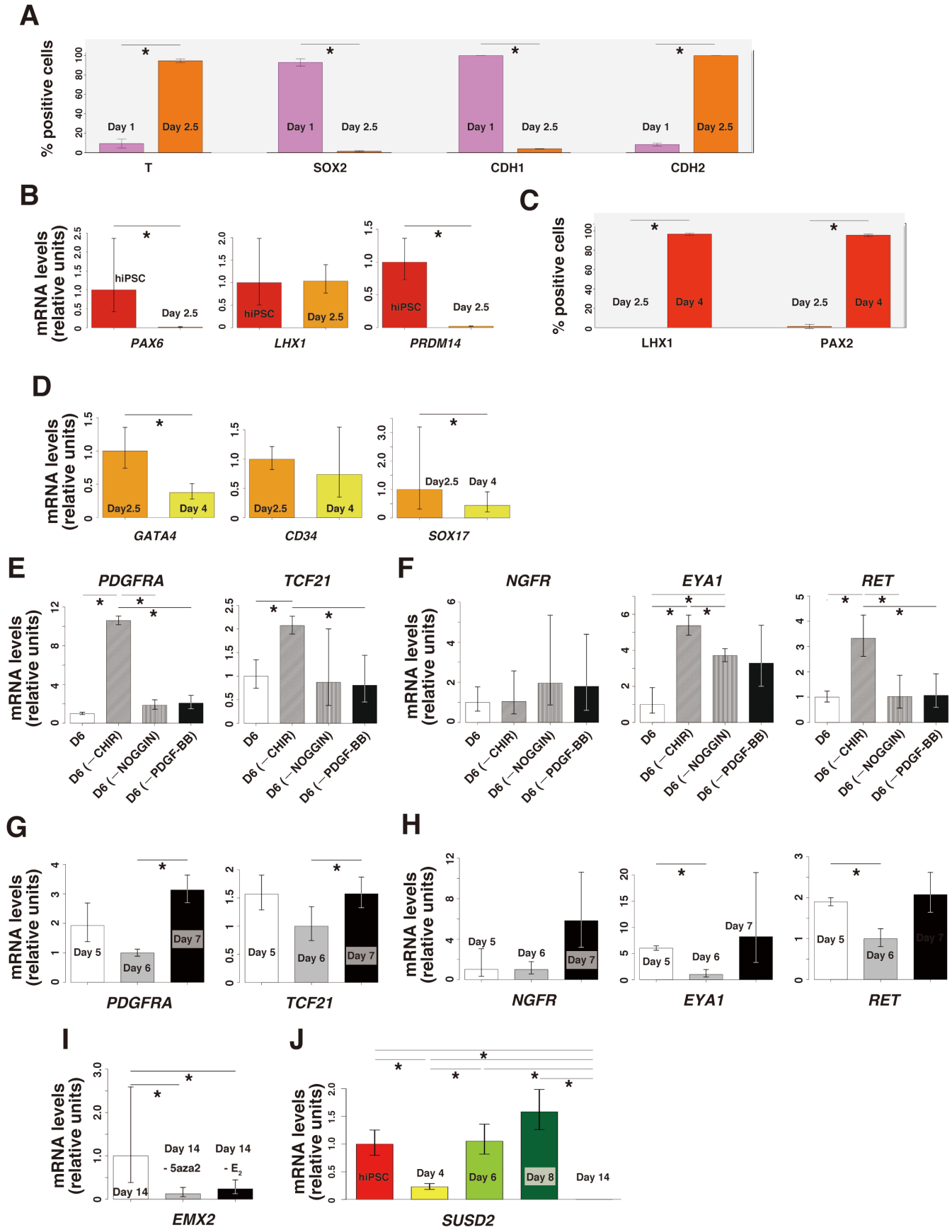

Supplemental Figure 2

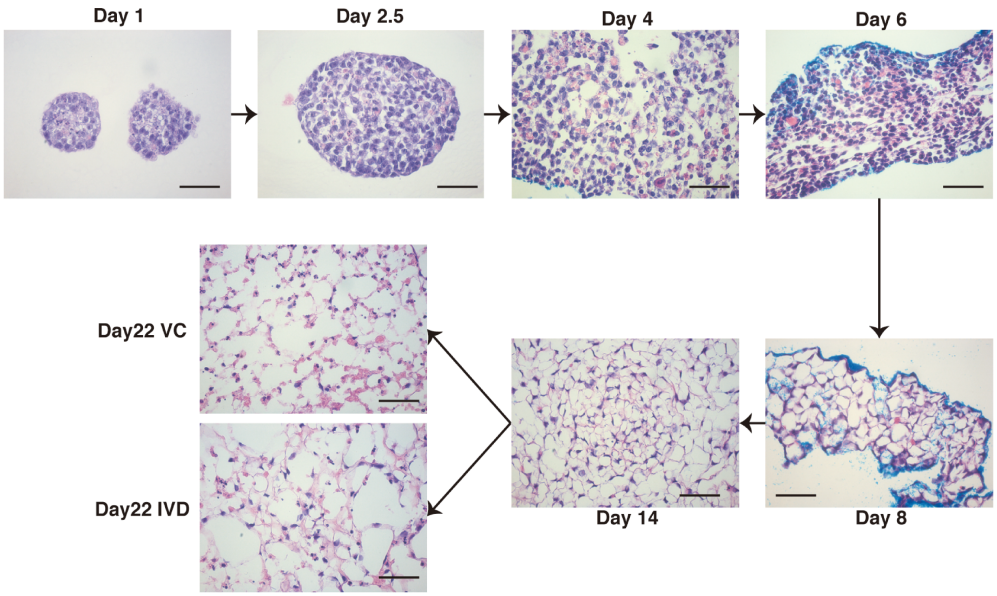

Supplemental Figure 3

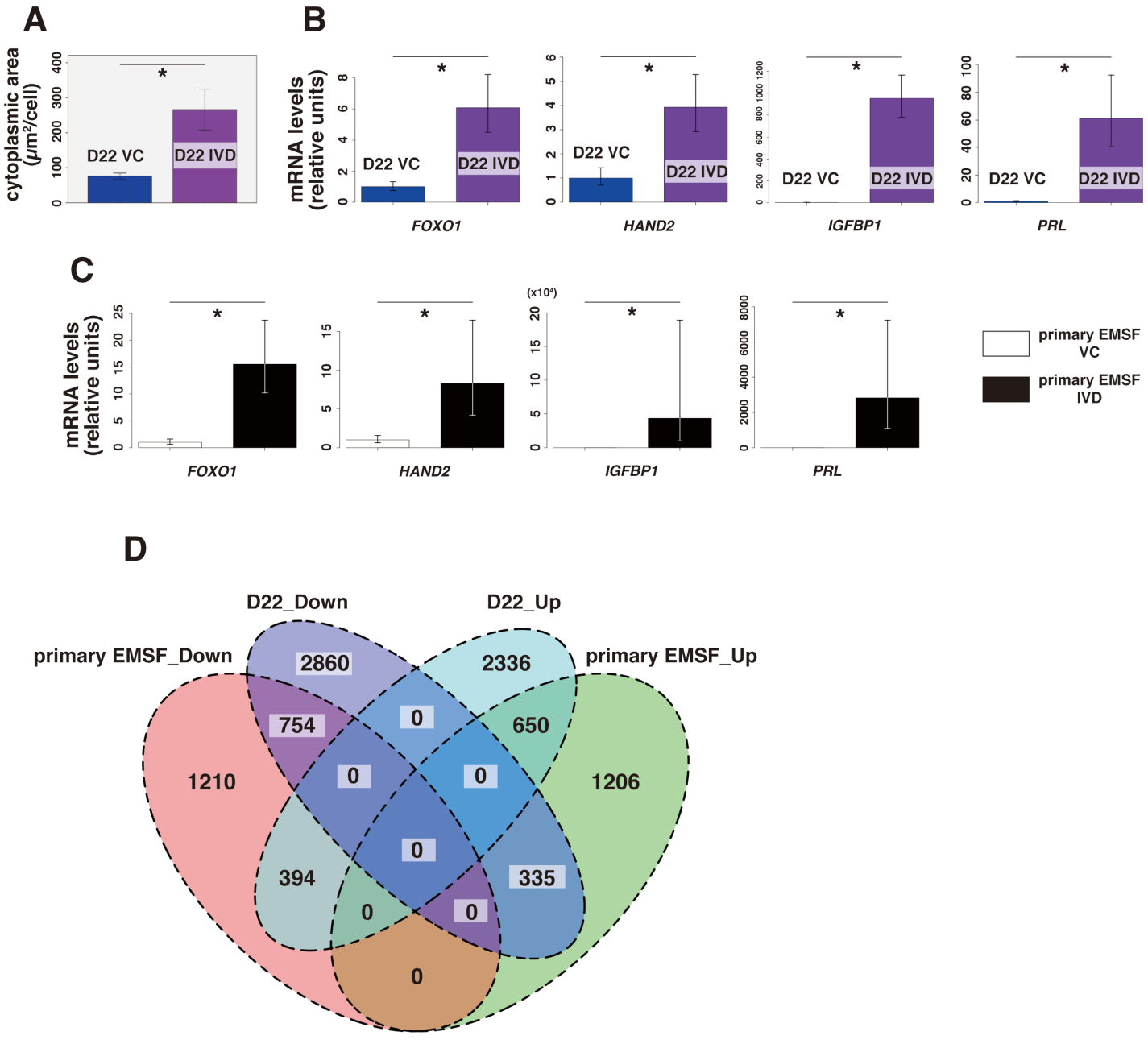

Supplemental Figure 4

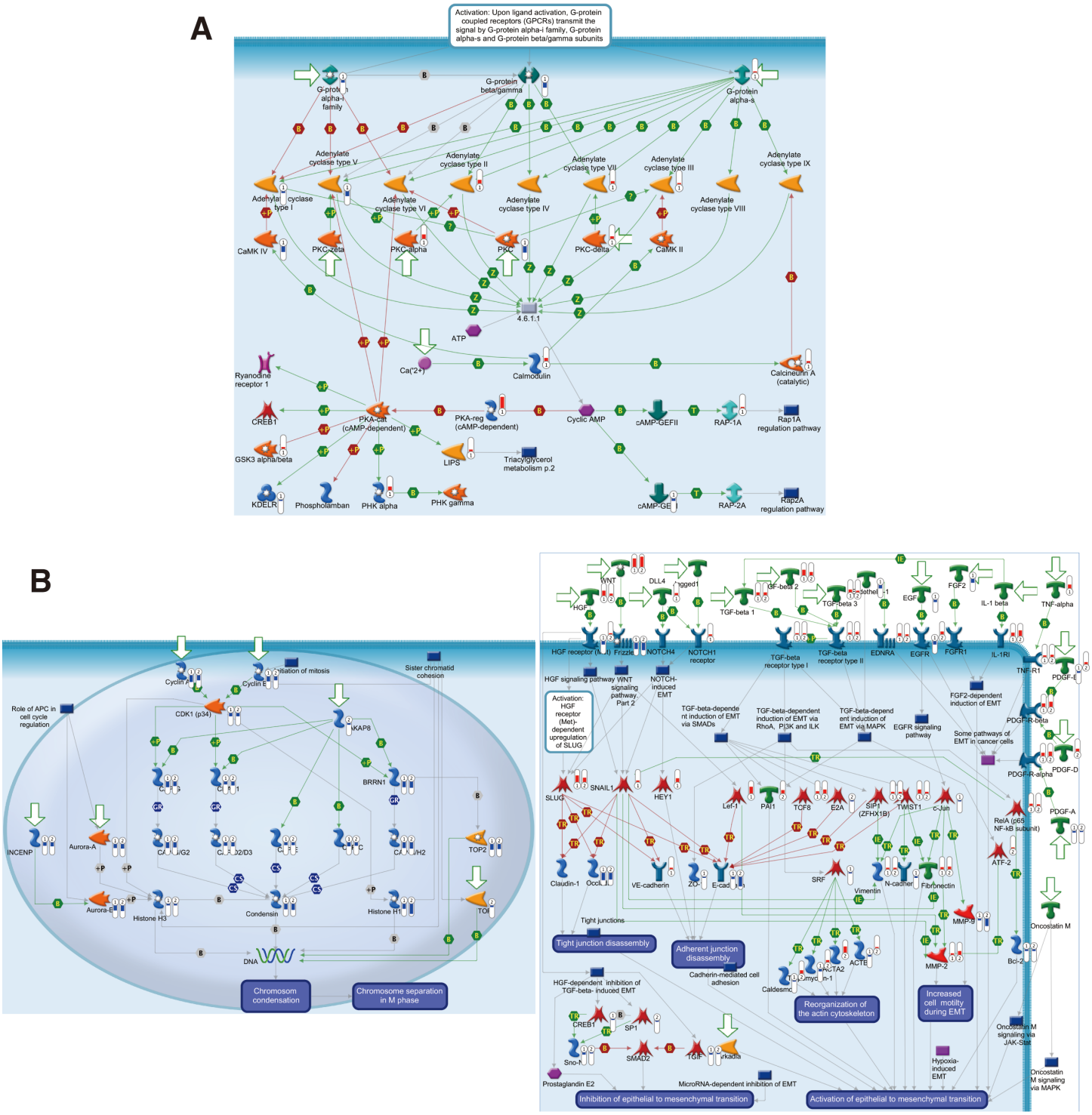

Supplemental Figure 5

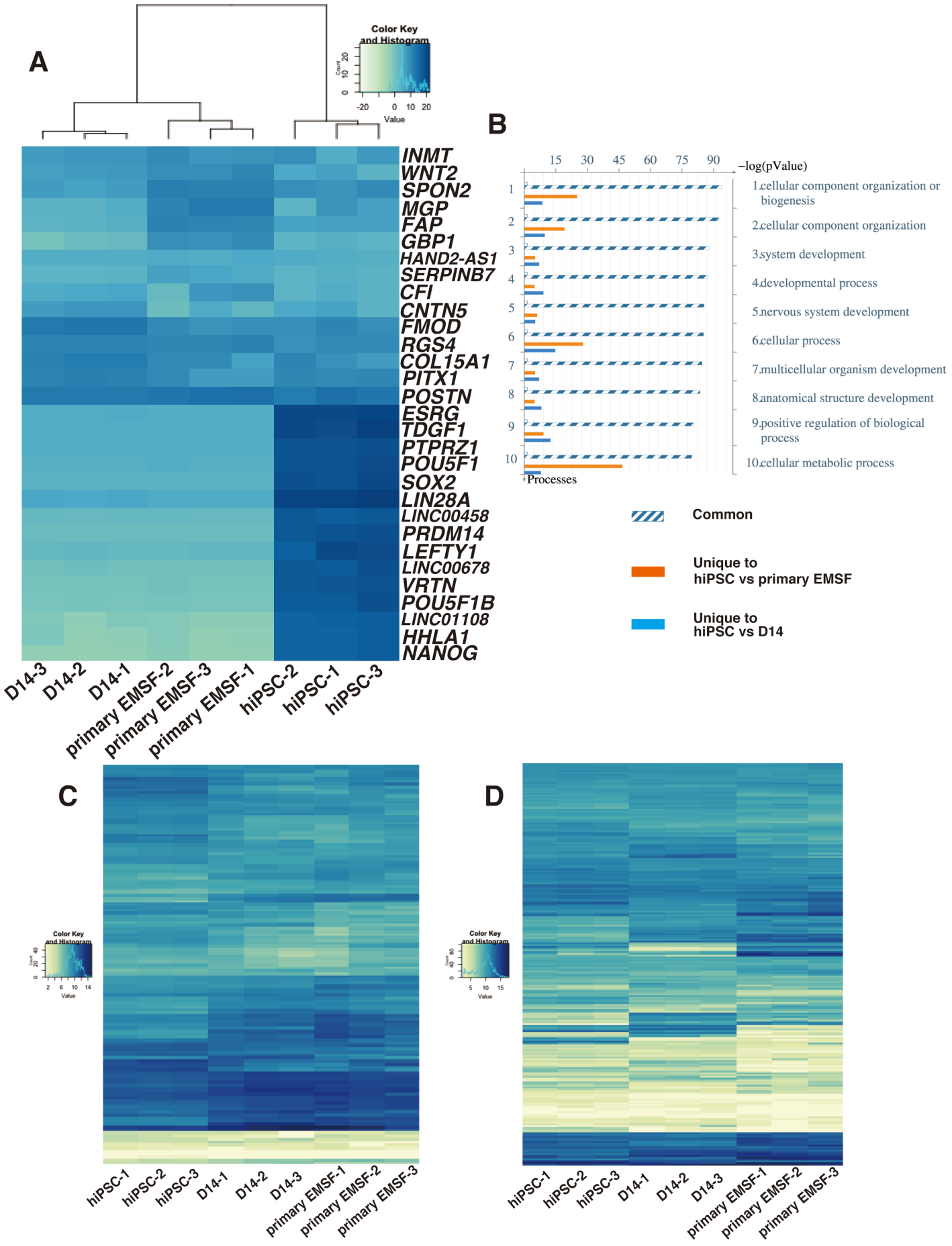

Supplemental Figure 6

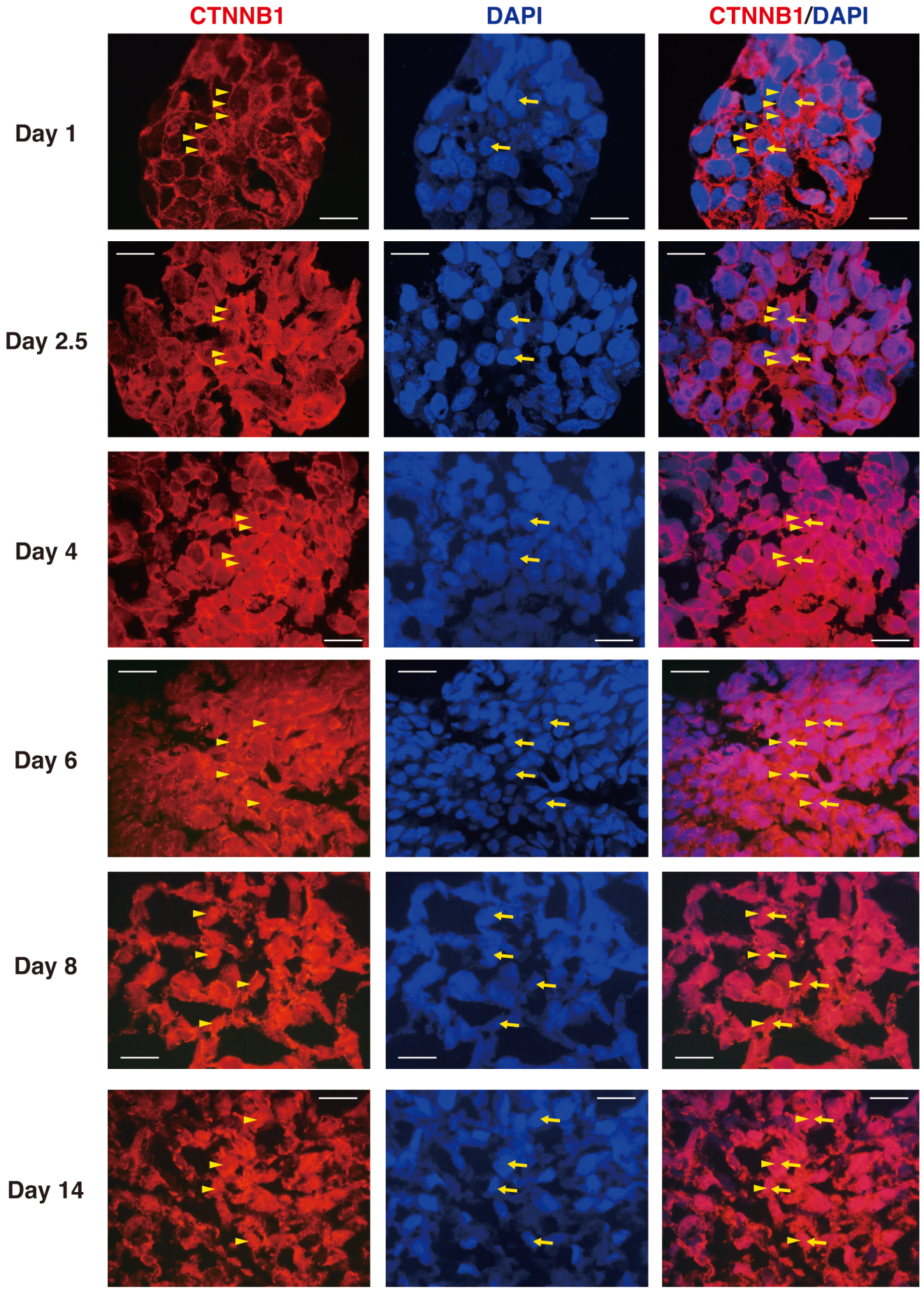

Supplementary Table 5: Primary antibodies used for flow cytometry

Antibody	**Company**	**Product number**	**Clone**	**Fluorochrome and isotype**	**Usage**
CD45	BD Biosciences	555485	HI30	APC-conjugated mouse IgG1	5 µl/1 × 10^6 cells
PDGFRA	BioLegend (San Diego, CA)	323506	16A1	PE-conjugated mouse IgG1	20 µl/1 × 10^6 cells
SUSD2	BioLegend	327406	W5C5	PE-conjugated mouse IgG1	5 µl/1 × 10^6 cells

Supplemental Table 6: List of primers used in qPCR

Target	Source	Product Id/Reference
ABRACL	Integrated DNA Technologies	Hs.PT.58.26763043
CD34	Integrated DNA Technologies	Hs.PT.56a.24708916
COL1A1	Thermo Fisher Scientific	Hs01076777_m1
EMX2	Integrated DNA Technologies	Hs.PT.58.39738222
EYA1	Integrated DNA Technologies	Hs.PT.58.39826997
FOXO1	Integrated DNA Technologies	Hs.PT.58.40005627
FN1	Integrated DNA Technologies	Hs.PT.58.40005963
GATA4	Thermo Fisher Scientific	Hs00171403_m1
HAND2	Integrated DNA Technologies	Hs.PT.58.4938123
HOXA10	Integrated DNA Technologies	Hs.PT.53a.20472403
HOXA11	Integrated DNA Technologies	Hs.PT.58.2064492
IGFBP	Integrated DNA Technologies	Hs.PT.58.3620731
ISL1	Integrated DNA Technologies	Hs.PT.58.2143768
KLF4	Integrated DNA Technologies	Hs.PT.58.45542593
LHX1	Integrated DNA Technologies	Hs.PT.58.3163761
NANOG	Integrated DNA Technologies	Hs.PT.58.21480849
NGFR	Integrated DNA Technologies	Hs.PT.58.4045496
NR5A1	Integrated DNA Technologies	Hs.PT.58.24264281
OSR1	Integrated DNA Technologies	Hs.PT.58.25056666
PAX2	Integrated DNA Technologies	Hs.PT.58.40853724
PAX6	Integrated DNA Technologies	Hs.PT.58.3002797
PDGFRA	Integrated DNA Technologies	Hs.PT.58.45699973
PGR	Thermo Fisher Scientific	Hs01556702_m1
PRDM14	Integrated DNA Technologies	Hs.PT.58.40121577
PRL	Integrated DNA Technologies	Hs.PT.58.3356588
RET	Integrated DNA Technologies	Hs.PT.58.4318912
SOX17	Integrated DNA Technologies	Hs.PT.58.24876513
SUSD2	Integrated DNA Technologies	Hs.PT.58.1294267
T	Integrated DNA Technologies	Hs.PT.58.1243965
TBP	Thermo Fisher Scientific	Hs99999910_m1

TBX6	Integrated DNA Technologies	Hs.PT.58.21333693
TCF21	Integrated DNA Technologies	Hs.PT.58.20883784
VIM	Integrated DNA Technologies	Hs.PT.58.38906895
ZFP42	Integrated DNA Technologies	Hs.PT.58.23001209

Supplemental Table 7: Primary antibodies used for immunostaining and Western blot

Antibody	Company	Product number	Clone	Appli-cation	Dilution	Retrieval (for IHC)	Incubation (for IHC)
ACTB	MilliporeSigma	A1978	AC-15	WB	1:10,000		
CDH1	Santa Cruz Biotechnology	sc-8426	G-10	IHC	1:50	ER1(20)= PH6	Leica Bond-Max Protocol F
CDH2	Thermo Fisher Scientific	33-3900	3B9	IHC	1:50	ER2(20)= PH9	Leica Bond-Max Protocol F
Type I collagen	SouthernBiotech (Birmingham, AL)	1310-01	Poly-clonal	IF, WB	1:30 (IF), 1:1,000 (WB)		
CTNNB1	BD Biosciences	610153	14	IF	1:100		
FOXO1	Cell Signaling Technology	14952	D7C1H	IHC, WB	1:100 (IHC), 1:1,000 (WB)	Ph6	Dako Autostainer plus 30/30
HOXA11	abcam (Cambridge, MA)	ab28699	Poly-clonal	IHC	1:200	ER1(20)= PH6	Leica Bond-Max Protocol F
HOXA11	Proteintech Group (Rosemont, IL)	55495-1-AP	Poly-clonal	WB	1:1,000		
ISL1	R&D Systems	AF1837	Poly-clonal	IF, WB	1:50 (IF), 1:200 (WB)		
LHX1	R&D Systems	MAB2725	320416	IHC, WB	1:200 (IHC), 1:1,000 (WB)	ER2(20)= PH9	Leica Bond-Max protocol F

NANOG	Thermo Fisher Scientific	PIPA1097	Poly-clonal	IHC, WB	1:200 (IHC), 1:1,000 (WB)	ER1(20)= PH6	Bond IHC Protocol F 15 min
PAX2	Thermo Fisher Scientific	71-6000	Poly-clonal	IHC, WB	1:150 (IHC), 1:1,000 (WB)	ER2(20)= PH9	Leica Bond-Max Protocol F H2O2 on the end
PDGFRA	Proteintech Group	60045-1-Ig	2C11B8	IHC, WB	1:100 (IHC), 1:1,000 (WB)	ER1(20)= Ph6	Leica Bond-Max protocol F
PGR	Agilent	M3569	PgR 636	IHC	1:100	ER1(20)	Leica Bond-Max Protocol PCF
PGR	Agilent	M356801-2	PgR 1294	WB	1:1,200		
PRLR	Cell Signaling Technology	M7018	D4A9	IHC, WB	1:200 (IHC), 1:100 (WB)	ER2(20)= PH9	Leica Bond-Max protocol PCF
SOX2	Cell Signaling Technology	2748	Poly-clonal	IHC, WB	1:100 (IHC), 1:1,000 (WB)	Ph6	Dako Autostainer plus Envision 30/15
T	Santa Cruz Biotechnology	sc-20109	Poly-clonal	IHC, WB	1:50 (IHC), 1:1,000 (WB)	ER1(20)= PH6	Leica Bond-Max Protocol F
VIM	Cell Signaling Technology	3932	Poly-clonal	WB	1:1,000		

Supplemental Figure 1. Assessment of cell-specific gene markers and cell morphology in EB during differentiation of hiPSC to EMSF. **(A)** Quantification of cells with positive immunofluorescence staining for T, SOX2, CDH1, and CDH2 in Day 1 and Day 2.5. Data represent mean ± SEM (N=3 independent experiments, *P<0.05, Student's t test for T and SOX2, Welch test for CDH1 and CDH2). **(B)** Quantitative RT-PCR comparing expression of *PAX6*, *LHX1*, and *PRDM14* in hiPSC and D2.5 EB. Genes are expressed in non-PS derivatives from EpiSCs. Error bars represent RQMin and RQMax (N=9 independent experiments, *P<0.05, Student's t test). **(C)** Quantification of cells with positive immunofluorescence staining for LHX1 and PAX2 in Day 2.5 and Day 4. Data represent mean ± SEM (N=3 independent experiments, *P<0.05, Student's t test for LHX1, Mann-Whitney test for PAX2). **(D-E)** Quantitative RT-PCR of coelomic epithelium (CE)-specific genes *PDGFRA* and *TCF21* **(D)** and non-CE derivative markers *NGFR*, *EYA*, and *RET* **(E)** in Day 6 EB. D6: D6 EB treated with CHIR, NOGGIN, and PDGF-BB; D6 (－CHIR): D6 EB treated with NOGGIN and PDGF-BB; D6 (－NOGGIN): D6 EB treated with CHIR and PDGF-BB; D6 (－PDGF-BB): D6 EB treated with CHIR and NOGGIN. Error bars represent RQMin and RQMax (N=3 independent experiments except for D6 (N=9 independent experiments), *P<0.05, Student's t test). **(F-G)** Quantitative RT-PCR of coelomic epithelium (CE)-specific genes *PDGFRA* and *TCF21* **(F)** and *NGFR*, *EYA*, and *RET* **(G)** in Day 5, 6, and 7 EB treated with CHIR, NOGGIN, and PDGF-BB. Error bars represent RQMin and RQMax (N=3 independent experiments except for D6 (N=9 independent experiments), *P<0.05, Student's t test). **(H)** Quantitative RT-PCR comparing expression of *GATA4*, *CD34*, and *SOX17* in D2.5 EB and D4 EB. Genes are expressed in non-IM derivatives from PS. Error bars represent RQMin and RQMax (N=9 independent experiments, *P<0.05, Student's t test). **(I)** Effect of withdrawal of 5aza2 or E_2 in mRNA expression level of *EMX2* in D14 EB. D14: D14 EB treated with 5aza2, CHIR, E_2, FGF9, and PDGF-BB; D14 - 5aza2: D14 EB treated with CHIR, E_2, FGF9, and PDGF-BB; D14 - E_2: D14 EB treated with 5aza2, CHIR, FGF9, and PDGF-BB for 6 days, between D8 and D14. Error bars represent RQMin and RQMax (N=3 independent experiments except for D14 (N=9 independent experiments), *P<0.05, Student's t test). **(J)** Quantitative RT-PCR comparing

expression of *SUSD2* in hiPSC, D4, D6, D8, and D14. Error bars represent RQMin and RQMax (N=9 independent experiments, *P<0.05, Student's t test).

Supplemental Figure 2. H&E staining of D1, D2.5, D4, D6, D8, D14, and D22 EB (IVD).

Supplemental Figure 3. In-vitro decidualization studies. **(A)** Quantification of cytoplasmic area in D22 VC and IVD. Data represent mean ± SEM (N=3 independent experiments, *P<0.05, Student's t test). **(B)** Quantitative RT-PCR of decidualization-specific genes *FOXO1*, *HAND2*, *IGFBP1*, and *PRL* in D22 VC and D22 IVD differentiated from clone 2 hiPSC. Error bars represent RQMin and RQMax (N=3 independent experiments, *P<0.05, Student's t test). **(C)** Quantitative RT-PCR of decidualization-specific genes *FOXO1*, *HAND2*, *IGFBP1*, and *PRL* in primary EMSF. Error bars represent RQMin and RQMax (N=3 independent experiments, *P<0.05, Student's t test). **(D)** Differentially expressed genes (DEGs) based on a comparison of RNA-seq data from D22 EB after IVD treatment and previous DNA microarray data from primary EMSF after IVD treatment (N=3 independent experiments, FDR adjusted p-value<0.05). The Venn diagrams show the total numbers of up- and downregulated genes identified in each comparison.

Supplemental Figure 4. Signaling pathways obtained from pathway enrichment analyses. **(A)** cAMP signaling pathway obtained from pathway analysis using MetaCore website based on DEGs in D22 IVD relative to vehicle control (N=3 independent experiments, FDR adjusted p-value<0.05). **(B)** Pathway maps obtained from pathway analysis using MetaCore based on DEGs in primary EMSF and D14 EB relative to hiPSC (N=3 independent experiments, FDR adjusted p-value<0.05). The pathway of chromosome condensation in prometaphase (left) and EMT pathway involving TGF and WNT/CTNNB1 signaling (right).

Supplemental Figure 5. Comparison of transcriptomes between hiPSC, hiPSC-derived EMSF, and primary EMSF. **(A)** Top 30 common DEGs in D14 and primary EMSF relative to hiPSC (N=3 independent experiments, FDR adjusted p-value<0.05). **(B)** Gene ontology

(GO) analysis using MetaCore (FDR < 0.05) performed on the same gene list used in **Figure 5D** (N=3 independent experiments, FDR adjusted p-value<0.05). The top 10 significantly enriched GO terms are shown with the -log of their FDR values on the x-axis. **(C)** Heatmap analysis comparing the expression of 133 cell cycle regulation genes in hiPSC, D14 EB, and primary EMSF (N=3 independent experiments). **(D)** Heatmap analysis comparing the expression of 232 genes that contributes to skeletal remodeling pathway and EMT pathway in hiPSC, D14 EB, and primary EMSF (N=3 independent experiments).

Supplemental Figure 6. Translocation of CTNNB1 during the differentiation of hiPSC. Single channel images of representative immunofluorescence for CTNNB1 in hiPSC, D2.5, D4, D6, D8, and D14 EB in Figure 7A were shown in this figure. Scale bars represent 20 μm. Yellow arrowheads indicate CTNNB1 staining. Yellow arrows indicate DAPI-positive cell nuclei.

Supplemental Table 1. List of pathways with FDR values obtained in the pathway enrichment analysis based on DEGs in D22 EB relative to vehicle control (top 200)

Supplemental Table 2. List of genes used in the heatmap analyses

Supplemental Table 3. List of pathways with FDR values obtained in the pathway enrichment analysis comparing DEGs in primary EMSF and D14 EB relative to hiPSC (top 200)

Supplemental Table 4. List of GO terms with FDR values obtained in the GO analysis comparing DEGs in primary EMSF and D14 EB relative to hiPSC (top 50)

Supplemental Table 5. List of antibodies used in the flow cytometry

Supplemental Table 6. List of primers used in qPCR

Supplemental Table 7. List of antibodies used in the immunostaining and western blots

SUPPLEMENTAL EXPERIMENTAL PROCEDURES

Differentiation

For all differentiation experiments, hiPSC grown on feeder layers of mitomycin C-treated MEFs were first dissociated by an enzymatic method with EDTA dissociation solution, and then incubated on gelatin-coated dishes for 30 min to remove MEFs. Then, the cells were dissociated into single cells by gentle pipetting after treatment with Accutase (Innovative Cell Technologies, San Diego, CA) for 20 min.

Cells were then plated at a density of 4.7 x 10^6 cells/well onto AggreWell400Ex (STEMCELL Technologies, Cambridge, MA) in hiPSC maintenance medium supplemented with 5 ng/ml recombinant human FGF2 and the ROCK inhibitor Y27632 10 mM (ApexBio Technology, Houston, TX) to form 4,700 embryoid bodies (EB) consisting of 1,000 cells. EB were harvested from AggreWell400Ex 24-32 hours after adding the hiPSC to the AggreWell400Ex, and plated at 2,350 EB/well in an ultra-low adherence 6-well plate (STEMCELL Technologies).

To induce PS and IM differentiation, a procedure described in Lam et al. (2014) was used. The media were changed to DMEM/F12 supplemented with 2 mM GlutaMAX, 100 IU/mL penicillin, 100 mg/mL streptomycin (Thermo Fisher Scientific), and CHIR (MedChemExpress, Monmouth Junction, NJ) for 36 hours to induce PS (D2.5 EB). EB were then treated with DMEM/F12 + 2 mM GlutaMAX + 1 x P/S + 100 ng/ml FGF2 + 1 mM retinoic acid (MilliporeSigma) for 36 hours to induce differentiation of IM (D4 EB).

For induction of CE, D4 EB were treated with basic differentiation medium (DMEM/F12 + 2.5% KnockOut Serum Replacement + 1 mM nonessential amino acids + 2 mM GlutaMAX + 0.55 mM 2-mercaptoethanol) supplemented with 3 μM CHIR, 5 ng/ml NOGGIN (PeproTech), and 10 ng/ml PDGF-BB (Thermo Fisher Scientific) for 2 days to produce CE (D6 EB). Controls were maintained in basic differentiation medium.

For induction of MD (D8 EB), the medium of D6 EB was changed to basic differentiation medium supplemented with 3 μM CHIR and 5 ng/ml NOGGIN for 2 days. To induce EMSF (D14 EB), D8 EB were treated with basic differentiation medium supplemented with 1 μM 5aza2 (MilliporeSigma), 3 μM CHIR, 10 ng/ml FGF-9 (R&D Systems, Minneapolis, MN), and 10 ng/ml PDGF-BB for 2 days, followed by the addition of 10^{-8}M E_2 (MilliporeSigma) for 4 days. Controls were maintained in basic differentiation medium.

To inhibit the canonical WNT/CTNNB1 pathway, D4, D6, and D8 EB were cultured without CHIR or treated with CTNNB1 inhibitors 5 μM IWP2 (R&D Systems, Minneapolis, MN) or 10 μM XAV939 (MilliporeSigma) in the presence of CHIR until D6, D8, and D14, respectively.

Flow cytometry analysis of D6 EB

D6 EB were dissociated into single cells by gentle pipetting after treatment with Accutase for 20 min. Dissociated D6 EB were resuspended at a concentration of 1×10^7 cells/ml in HBSS containing 2% KnockOut Serum Replacement (staining medium), and incubated with the PE-conjugated antibody against PDGFRA for 30 min at 4°C in the dark. The cells were then washed twice with cold staining medium, and fixed with 0.5% paraformaldehyde (Electron Microscopy Sciences, Hatfield, PA) in PBS overnight at 4°C in the dark, then washed with PBS, and resuspended in 3 μM 4’,6-diamidino-2-phenylindole (DAPI; Thermo Fisher Scientific) to label nonviable cells. Finally, the cells were subjected to flow cytometry analysis using BD FACSAria Cell Sorter (BD Biosciences (San Jose, CA)) to examine the percentage of PDGFRA+ cells. Forward scatter, side scatter, and DAPI gating excluded debris, doublets, and dead cells.

Isolation and culture of primary EMSF

Enzymes for tissue processing were obtained from MilliporeSigma. Cell culture media, trypsin, and supplements were from Thermo Fisher Scientific. Homogenous populations of primary EMSF were isolated from endometrial tissue as previously described (Ryan et al., 1994). Briefly, stroma and glandular fragments were dissected from adjacent tissue,

minced, and digested with collagenase and DNase at 37°C for 30 min. Samples were then treated with collagenase (MilliporeSigma), DNase (MilliporeSigma), protease (MilliporeSigma), and hyaluronidase (MilliporeSigma) at 37°C for an additional 30 min. Epithelial cells were eliminated by progressive filtration through sterile 70- and 20-μm sieves, and human EMSF were dispensed into 100-mm dishes for adherent growth and maintained in DMEM/F12 supplemented with 10% fetal bovine serum (FBS) (VWR International, Radnor, PA), 100 IU/mL penicillin, 100 mg/mL streptomycin, and 2.5 mg/mL amphotericin B (Thermo Fisher Scientific). Cells were maintained and grown in a humidified atmosphere with 5% CO_2 at 37°C, and medium was replenished every 48 h.

Isolation of SUSD2+ human eMSC

eMSC were isolated using flow cytometry according to the previously published protocol (Masuda et al., 2012). Briefly, dissociated EMSF were resuspended at a concentration of 2×10^6 cells/ml in HBSS containing 2% FBS (staining medium), and incubated with fluorescently labeled antibodies against CD45 and SUSD2 for 30 min at 4°C in the dark. The antibodies used are listed in Supplemental Table 5. The cells were then washed twice with cold staining medium and resuspended in 1 μg/ml propidium iodide (PI; MilliporeSigma) to label nonviable cells. Finally, the cells were subjected to fluorescent activated cell sorting (FACS) using BD FACSAria Cell Sorter to isolate SUSD2+ cells. Forward scatter, side scatter, and PI gating excluded erythrocytes, debris, doublets, and dead cells. Leukocytes (CD45+) were also excluded by electronic gating.

In vitro decidualization (IVD)

IVD regimens followed previous protocols with some modifications (Kim et al., 2007). Briefly, the medium was switched to phenol red-free DMEM/F12 media (Thermo Fisher Scientific) supplemented with 2% charcoal-dextran-stripped FBS and antibiotics after differentiation. Controls were maintained in this reduced medium, while IVD treatment consisted of 1 mM MPA (MilliporeSigma), 10^{-8} M E_2 (MilliporeSigma), and 0.3 mM cAMP (BIOLOG, Bremen Germany). Cells underwent 8-day IVD treatments.

RNA extraction, reverse transcription, and quantitative RT-PCR

Total RNAs were isolated from hiPSC, D2.5, D4, D6, D8, D14, D22 VC, D22 IVD EB, and primary EMSF using the RNeasy Mini Kit (Qiagen, Germantown, MD). The concentration of total RNA was measured by NanoDrop (Thermo Fisher Scientific). 266 ng of RNA was reverse-transcribed using the SUPERSCRIPT VILO (Thermo Fisher Scientific) to produce cDNA. For primers and probes, TaqMan gene expression assays (Thermo Fisher Scientific) or PrimeTime qPCR Assay (Integrated DNA Technologies, Coralville, IA) was used. RT-PCR reactions were run in duplicate using 3.8 ng cDNA, 500 nM primers, 250 nM probe, and TaqMan Universal PCR Master Mix (Thermo Fisher Scientific). Quantitative RT-PCR was performed using QuantStudio 12K Flex (Thermo Fisher Scientific). The cycling conditions were: 50°C for 2 min, 95°C for 10 min, and 40 cycles of 95°C for 15 s followed by 60°C for 1 min.

Expression levels were calculated by applying the comparative cycle threshold (Ct) method. Relative expression levels were normalized to the geometric mean of three housekeeping genes, RPL7, RPL15, and TBP, using ExpressionSuite Software Version 1.0.4 (Thermo Fisher Scientific). All qRT-PCR experiments were carried out with a non-template control. Primer information is provided in Supplemental Table 6.

Immunostaining of EB

EB were fixed with 4% paraformaldehyde in PBS for 30 min at RT, then washed three times in PBS. The EB were embedded in paraffin and sectioned at 5 µm. Richard-Allan Scientific HistoGel Specimen Processing Gel (Thermo Fisher Scientific) was used to encapsulate and retain D1, D2.5, and D4 EB during histological processing according to the manufacturer's protocol.

After deparaffinization and rehydration, the EB were then either stained with hematoxylin (MilliporeSigma) and eosin (VWR), or for individual proteins using primary antibodies and indirect immunostaining. See Supplemental Table 7 for antibody information. Immunofluorescence was performed for detection of type I collagen, CTNNB1, ISL1, and MME. Briefly, after antigen retrieval by heating in Target Retrieval Solution (Agilent, Santa Clara, CA), non-specific staining between the primary antibodies and the

tissue was blocked by incubating in blocking buffer (1% horse serum (VWR) in PBS) for 30 minutes at RT. The primary antibody was diluted in incubation buffer (1% FBS, 0.3% Triton X-100 (MilliporeSigma), and 0.01% sodium azide (MilliporeSigma) in PBS and applied to the sections. After incubation at 4°C overnight, the sections were washed with PBS and incubated with an anti-mouse Cy3 antibody (Jackson ImmunoResearch Laboratories, West Grove, PA) or anti-goat Alexa Fluor 488-conjugated antibody (Thermo Fisher Scientific) at RT for 1 hour. Nuclei were counterstained with DAPI (Thermo Fisher Scientific) at RT for 5 min.

For detection of other proteins, 3,3'-Diaminobenzidine (DAB) immunohistochemistry was performed using Dako Autostainer Plus (Agilent) or BOND-MAX Fully automated IHC and ISH (Leica Biosystems, Buffalo Grove, IL) with Bond Polymer Refine Detection (Leica Biosystems). Sections were mounted in ProLong Gold Antifade Mountant (Thermo Fisher Scientific) for immunofluorescence or Micromount (Leica Biosystems) for DAB immunohistochemistry and examined using an Automated Upright Microscope System for Life Science Research Leica DM5000 B (Leica Biosystems). Quantification was performed by counting three random fields at x100 magnification. Cytoplasmic volume was assessed on H&E staining and quantified as a two-dimensional area using ImageJ (Schneider et al., 2012). The real size of the image obtained at x100 magnification is 14,675.9 μm^2, and this corresponds to 7,990,272 pixels on ImageJ. Therefore, the cytoplasmic area was calculated using the following formula:

Cytoplasmic area (μm^2) = (number of pixels in cytoplasm) * 14,675.9 / 7,990,272

Cytoplasmic area per cell was obtained using cytoplasmic area and the cell number in the image to assess the average cytoplasmic volume of cells, and used for statistical analyses.

Preparation of protein and immunoblotting

Whole cell lysates were prepared by washing cells with PBS, followed by lifting and homogenizing the cells in RIPA buffer (50 mM Tris pH 7.6 (MilliporeSigma), 150 mM NaCl, 0.1% SDS, 0.5% sodium deoxycholate (MilliporeSigma), 1% IGEPAL CA-630

(MilliporeSigma)) supplemented with protease inhibitor cocktail (MilliporeSigma). Lysates were cleared by centrifugation at 14,000 x g for 10 min. Equal amounts of protein (20 µg) were resolved on NuPAGE Novex 4–12% bis-Tris Gels (Thermo Fisher Scientific). Transfer and membrane blocking were performed as previously described (Dyson et al., 2008). Incubation with primary antibodies (Supplemental Table 7) was performed at 4°C in 5% nonfat milk (Bio-Rad, Hercules, California) overnight. The membranes were then washed and incubated with the anti-mouse (Cell Signaling Technology, Danvers, MA), anti-rabbit (Cell Signaling Technology), or anti-goat (Santa Cruz Biotechnology, Dallas, TX) HRP-conjugated antibody for 1 h. Detection was performed using HyGLO Quick Spray Chemiluminescent HRP Antibody Detection Reagent (Denville Scientific, Holliston, MA), Luminata Crescendo HRP substrate (MilliporeSigma), or SuperSignal West Femto Maximum Sensitivity Substrate (Thermo Fisher Scientific). ImageJ software (National Institutes of Health, Bethesda, MD) was used to quantify immunoblot densitometry.

Enzyme-linked immunosorbent assay (ELISA)

IGFBP-1 levels in the conditioned media from D22 EB were assayed using ELISA kits from Alpha Diagnostic International (San Antonio, TX) according to the manufacturer's instruction. The minimum IGFBP-1 concentration detectable using this assay is 0.4 µg/L. Intra-assay coefficients of variation were 2.4–3.4% and inter-assay coefficients of variation were 5.0–7.4%. IGFBP-1 protein concentrations were normalized to genomic DNA content in each well. AllPrep DNA/RNA Mini Kit (Qiagen) was used to extract genomic DNA from EB. Genomic DNA content was measured using NanoDrop.

RNA-seq

For RNA-seq library preparation of hiPSC, D4, D6, D8, D14, D22 VC, D22 IVD, primary EMSF, and eMSC, DNA contaminants were digested with RapidOut DNA Removal Kit (Thermo Fisher Scientific). Total RNA quality was assessed using an Agilent Bioanalyzer 2100. RNA-seq libraries were constructed using KAPA Stranded RNA-Seq Kit with RiboErase (KAPA Biosystems, Wilmington, MA) following the manufacturer’s protocol. The ribosome RNAs were duplexed to DNA oligos and digested by RNase H treatment from

~500 ng DNAse-treated total RNA. Following purification, total RNA without ribosomal RNA was fragmented into small pieces using heat (94°C for 6 minutes) in the presence of Mg^{2+}. Under this condition, the average fragment length is 352 bp. Reverse transcriptase and random primers were used to copy the cleaved RNA fragments into first strand cDNA. The second strand cDNA was synthesized using DNA Polymerase I and dUTP in place of dTTP. These cDNA fragments then went through an A-tailing process, which adds dAMP to the 3′-ends of the cDNA library fragments, and adapter ligation, where double-stranded DNA adapters with 3′-dTMP overhangs are ligated to A-tailed library insert fragments. These products were then purified and enriched with 15 cycles of PCR to create the final cDNA library. The concentration of RNA libraries was measured by Qubit 3.0 Fluorometer (Thermo Fisher Scientific) and Qubit dsDNA Assay Kit (Thermo Fisher Scientific) following the manufacturer's protocol. The quality of RNA-seq library was measured by Agilent Bioanalyzer 2100. Three RNA samples from different experiments were used for constructing libraries for each stage.

cDNA libraries were sequenced as single-end, 75 base-length reads on an Illumina NextSeq 500 instrument (Illumina, San Diego, CA) with an average read count of 37 million reads per sample. Initial base calling and quality filtering of the RNA-seq reads generated with the Illumina analysis pipeline (fastQ format) were performed with the FastxToolkit (http://hannonlab.cshl.edu/fastx_toolkit/) and adapters trimmed by using CutAdapt (https://cutadapt.readthedocs.org/en/stable/). Reads were mapped (STAR v2.5.3a; https://github.com/alexdobin/STAR/archive/2.5.3a.tar.gz) to the reference genome (from Ensembl, v78; http://www.ensembl.org/index.html; Homo_sapiens.GRCh38.dna.primary_assembly.fa using Homo_sapiens.GRCh38.78.gtf as annotation).

Quantification and Statistical Analysis

Data analysis

For quantitative RT-PCR, relative quantification (RQ) (= $2^{-\Delta\Delta Ct}$) was obtained and a two-sample t-test was performed for statistical analysis using ExpressionSuite Software Version 1.0.4 (Thermo Fisher Scientific). Results are expressed as RQ with a range of

possible RQ values defined by the standard error (RQ min and max). For image analyses, immunoblot densitometry, and ELISA, distribution of each sample was assessed with the Shapiro-Wilk test. When the distributions of both samples were normal their dispersions were assessed with the Levene test. We compared homoscedastic samples using a two-sample t-test or for heteroscedastic samples, we used the Welch test. When at least either of the samples was not normally-distributed, they were compared using the Mann-Whitney test. IBM SPSS Statistics for Macintosh version 21.0 (IBM Corp., Armonk, NY) was used for these analyses. Results are expressed as means ± SEM.

For RNA-seq, differential expression P-values were calculated after normalizing expression values using DEseq2 (Love et al., 2014) (https://bioconductor.org/packages/release/bioc/html/DESeq2.html), an R package available through Bioconductor. R version 3.3.3 (R Development Core Team, 2014) was used for R-based analyses. P-values for expression differences between samples were then calculated in DEseq2 with a negative binomial distribution for gene expression. Finally, FDR (false discovery rate) for each P-value was calculated by DEseq2 using the Benjamini-Hochberg method.

PCA plot and hierarchical clustering with heatmap and dendrogram were generated using the R package “gplots.” Venn diagrams were generated using the R package “VennDiagram.”

For pathway enrichment analysis and GO analysis among different samples, MetaCore website (https://portal.genego.com) were used.

Reference

Dyson, M.T., Jones, J.K., Kowalewski, M.P., Manna, P.R., Alonso, M., Gottesman, M.E., and Stocco, D.M. (2008). Mitochondrial A-kinase anchoring protein 121 binds type II protein kinase A and enhances steroidogenic acute regulatory protein-mediated steroidogenesis in MA-10 mouse leydig tumor cells. Biology of reproduction *78*, 267-277.

Kim, J.J., Taylor, H.S., Lu, Z., Ladhani, O., Hastings, J.M., Jackson, K.S., Wu, Y., Guo, S.W., and Fazleabas, A.T. (2007). Altered expression of HOXA10 in endometriosis: potential role in decidualization. Molecular human reproduction *13*, 323-332.

Lam, A.Q., Freedman, B.S., Morizane, R., Lerou, P.H., Valerius, M.T., and Bonventre, J.V. (2014). Rapid and efficient differentiation of human pluripotent stem cells into intermediate mesoderm that forms tubules expressing kidney proximal tubular markers. Journal of the American Society of Nephrology : JASN *25*, 1211-1225.

Love, M.I., Huber, W., and Anders, S. (2014). Moderated estimation of fold change and dispersion for RNA-seq data with DESeq2. Genome biology *15*, 550.

Masuda, H., Anwar, S.S., Buhring, H.J., Rao, J.R., and Gargett, C.E. (2012). A novel marker of human endometrial mesenchymal stem-like cells. Cell transplantation *21*, 2201-2214.

R Development Core Team (2014). R: A language and environment for statistical computing (Vienna, Austria: R Foundation for Statistical Computing).

Ryan, I.P., Schriock, E.D., and Taylor, R.N. (1994). Isolation, characterization, and comparison of human endometrial and endometriosis cells in vitro. The Journal of clinical endocrinology and metabolism *78*, 642-649.

Schneider, C.A., Rasband, W.S., and Eliceiri, K.W. (2012). NIH Image to ImageJ: 25 years of image analysis. Nature methods *9*, 671-675.